haematologica
Journal of the Ferrata Storti Foundation

Genome-scale clustered regularly interspaced short palindromic repeats screen identifies nucleotide metabolism as an actionable therapeutic vulnerability in diffuse large B-cell lymphoma

by Nicholas Davies, Tegan Francis, Ceri Oldreive, Maria Azam, Jordan Wilson, Philip J. Byrd, Megan Burley, Archana Sharma-Oates, Peter Keane, Sael Alatawi, Martin R. Higgs, Zbigniew Rudzki, Maha Ibrahim, Tracey Perry, Angelo Agathanggelou, Anne-Marie Hewitt, Edward Smith, Constanze Bonifer, Mark O'Connor, Josep V. Forment, Paul G. Murray, Eanna Fennell, Gemma Kelly, Catherine Chang, Grant S. Stewart, Tanja Stankovic, Marwan Kwok, and Alexander Malcolm Taylor

Received: October 4, 2023.
Accepted: May 24, 2024.

Citation: Nicholas Davies, Tegan Francis, Ceri Oldreive, Maria Azam, Jordan Wilson, Philip J. Byrd, Megan Burley, Archana Sharma-Oates, Peter Keane, Sael Alatawi, Martin R. Higgs, Zbigniew Rudzki, Maha Ibrahim, Tracey Perry, Angelo Agathanggelou, Anne-Marie Hewitt, Edward Smith, Constanze Bonifer, Mark O'Connor, Josep V. Forment, Paul G. Murray, Eanna Fennell, Gemma Kelly, Catherine Chang, Grant S. Stewart, Tanja Stankovic, Marwan Kwok, and Alexander Malcolm Taylor. Genome-scale clustered regularly interspaced short palindromic repeats screen identifies nucleotide metabolism as an actionable therapeutic vulnerability in diffuse large B-cell lymphoma.
Haematologica. 2024 June 6. doi: 10.3324/haematol.2023.284404 [Epub ahead of print]

Genome-scale clustered regularly interspaced short palindromic repeats screen identifies nucleotide metabolism as an actionable therapeutic vulnerability in diffuse large B-cell lymphoma

*Nicholas Davies[1], *Tegan Francis[1], Ceri Oldreive[1], Maria Azam[1], Jordan Wilson[1], Philip J. Byrd[1], Megan Burley[1], Archana Sharma-Oates[2], Peter Keane[1], Sael Alatawi[1,3], Martin R. Higgs[1], Zbigniew Rudzki[4], Maha Ibrahim[1,5], Tracey Perry[1], Angelo Agathanggelou[1], Anne-Marie Hewitt[1], Edward Smith[1], Constanze Bonifer[1], Mark O'Connor[6], Josep V. Forment[6], Paul G. Murray[7], Eanna Fennell[7], Gemma Kelly[8], Catherine Chang[8], Grant S. Stewart[1], Tatjana Stankovic[1], Marwan Kwok[1,9], and Alexander Malcolm Taylor[1]

[1]Institute of Cancer and Genomic Sciences, University of Birmingham, Birmingham, UK
[2]School of Biosciences, University of Birmingham, Birmingham, UK
[3]Department of Medical Laboratory Technology, Faculty of Applied Medical Sciences, University of Tabuk, Tabuk, Saudi Arabia
[4]Department of Histopathology, University Hospitals Birmingham NHS Foundation Trust, Birmingham, UK
[5]South Egypt Cancer Institute, Assiut University, Egypt
[6]Bioscience Oncology R&D, AstraZeneca, Cambridge, UK
[7]School of Medicine, Bernal Institute, Health Research Institute & LDCRC, University of Limerick, Limerick, Ireland
[8]Blood Cells and Bood Cancer Division, The Walter and Eliza Hall Institute of Medical Research, Victoria, Australia
[9]Centre for Clinical Haematology, Queen Elizabeth Hospital Birmingham, Birmingham, UK

Running heads: Targeting nucleotide metabolism in DLBCL

Corresponding authors:

1. Alexander Malcolm Taylor, Institute of Cancer and Genomic Sciences, University of Birmingham, Birmingham, UK, B15 2TT; e-mail: a.m.r.taylor@bham.ac.uk; Tel: +44 121 4144488

2. Marwan Kwok, Institute of Cancer and Genomic Sciences, University of Birmingham, Birmingham, UK, B15 2TT, e-mail: m.kwok@bham.ac.uk; Tel: +44 121 4144496

3. Tatjana Stankovic, Institute of Cancer and Genomic Sciences, University of Birmingham, Birmingham, UK, B15 2TT; e-mail: t.stankovic@bham.ac.uk; Tel: +44 121 4144496

Authors' contributions: ND and TF contributed equally as co-first authors'. ND, TF, CO, MA, JW. PJB, MB, MH, RZ, MI, TP, AA, A-MH, ES, GK and CC performed experiments; ND, TF, CO, AS-O, PK, SA, MH, CB, PGM, EF and MK analyzed results; ND, TF, PJB, MO'C, JVF, GSS, TS and AMT designed the research; ND, TF, CO, TS, MK, and AMT wrote the paper.

Data sharing statement: RNA-seq and CRISPR data are available at GEO: https://www.ncbi.nlm.nih.gov/geo/query/acc.cgi?acc=GSE215877.

Acknowledgments: We thank Mike Griffiths (West Midlands Regional Genetics Laboratory) and Robert Hollows (Institute of Cancer and Genomic Sciences) for their expertize with data analysis; Paloma Garcia (Institute of Cancer and Genomic Sciences), Rachel Bayley (Institute of Cancer and Genomic Sciences) and Clare Shannon-Lowe (Institute of Immunology and Immunotherapy) for experimental assistance; and the University of Birmingham Genomics Sequencing and Flow Cytometry Services for analytical help.

Funding: This work was supported by grants from CRUK (Ref: C20807/A2864 and C17183/A23303), Bloodwise UK (Programme grant 11045) and Action for A-T (Ref: 17-1192). C.B. was supported by grants from MRC and BCUK. P.M. was also supported in part by a European Regional Development Fund Project (ENOCH: CZ.02.1.01/0.0/0.0/16_019/0000868). M.K. is a Cancer Research UK Clinician Scientist.

Competing Interests: MO'C and JVF are full-time employees and shareholders at AstraZeneca. The other authors declare no competing interests.

Abstract

Diffuse large B-cell lymphoma (DLBCL) is the most common malignancy that develops in patients with ataxia-telangiectasia, a cancer-predisposing inherited syndrome characterized by inactivating germline *ATM* mutations. *ATM* is also frequently mutated in sporadic DLBCL. To investigate lymphomagenic mechanisms and lymphoma-specific dependencies underlying defective *ATM*, we applied ribonucleic acid (RNA)-seq and genome-scale loss-of-function clustered regularly interspaced short palindromic repeats (CRISPR)/Cas9 screens to systematically interrogate B-cell lymphomas arising in a novel murine model ($Atm^{-/-}nu^{-/-}$) with constitutional *Atm* loss, thymic aplasia but residual T-cell populations. $Atm^{-/-}nu^{-/-}$ lymphomas, which phenotypically resemble either activated B-cell-like or germinal center B-cell-like DLBCL, harbor a complex karyotype, and are characterized by MYC pathway activation. In $Atm^{-/-}nu^{-/-}$ lymphomas, we discovered nucleotide biosynthesis as a MYC-dependent cellular vulnerability that can be targeted through the synergistic nucleotide-depleting actions of mycophenolate mofetil (MMF) and the WEE1 inhibitor, adavosertib (AZD1775). The latter is mediated through a synthetically lethal interaction between RRM2 suppression and MYC dysregulation that results in replication stress overload in $Atm^{-/-}nu^{-/-}$ lymphoma cells. Validation in cell line models of human DLBCL confirmed the broad applicability of nucleotide depletion as a therapeutic strategy for MYC-driven DLBCL independent of *ATM* mutation status. Our findings extend current understanding of lymphomagenic mechanisms underpinning *ATM* loss and highlight nucleotide metabolism as a targetable therapeutic vulnerability in MYC-driven DLBCL.

Introduction

Dysregulation of the *MYC* proto-oncogene represents a fundamental mechanism underpinning pathogenesis in high-grade B-cell non-Hodgkin lymphoma (B-NHL).[1] In diffuse large B-cell lymphoma (DLBCL), the most common form of high-grade B-NHL,[2] *MYC* overexpression and chromosomal translocations, present in up to 40% and 20% of DLBCL respectively, confer inferior outcomes with standard rituximab-based chemoimmunotherapy.[3] Moreover, concurrent overexpression of MYC and BCL-2 defines double-expressor DLBCL,[4,5] while translocations of *MYC* with *BCL2* and/or *BCL6* characterize double/triple-hit lymphoma,[6,7] both associated with dismal prognosis and poor response to standard chemoimmunotherapeutic approaches.[4,5,7,8]

In addition to *MYC* disruption, recent next-generation sequencing efforts have revealed numerous other genomic events, unravelling a hitherto unrecognized level of genetic heterogeneity in DLBCL and other high-grade B-NHL.[9] Furthermore, besides acquired somatic alterations that fuel clonal evolution,[10] there is increasing recognition of germline genetic alterations as important predisposing factors for B-cell lymphomagenesis.[11] Understanding the therapeutic vulnerability associated with these genetic alterations is essential for devising novel therapeutic strategies with potential to improve clinical outcome. In this regard, the tumor suppressor gene ataxia-telangiectasia mutated (*ATM*) is recurrently mutated in 8%-21% of sporadic DLBCL.[9,10,12,13] Moreover, high-grade B-NHL, particularly DLBCL, is the most frequent cancer type seen in individuals with ataxia-telangiectasia (A-T),[14,15] an inherited cancer predisposition syndrome caused by biallelic inactivating germline *ATM* mutations.[16] ATM plays a critical role in the maintenance of genome integrity through mediating deoxyribonucleic acid (DNA) repair, cell cycle arrest and/or apoptosis in response to DNA double-strand breaks.[17] Beyond the DNA damage response, ATM participates in multifaceted cellular processes including regulation of chromatin remodeling, oxidative stress response, mitochondrial metabolism and autophagy.[17] Despite *in vivo* evidence substantiating the role of *ATM* loss as a driver of DLBCL,[18] its pathological consequence has not been fully elucidated. Moreover, little is known about the resultant cellular vulnerabilities that could be exploited for therapeutic targeting.

To address this issue, we combined ribonucleic acid (RNA)-seq and genome-scale clustered regularly interspaced short palindromic repeats (CRISPR)/Cas9 screens to systematically interrogate pathogenic mechanisms and cellular dependencies within a novel murine model of DLBCL harboring constitutional *Atm* loss. We uncovered distinct transcriptional alterations associated with *Atm* loss that result in MYC activation and identified nucleotide biosynthesis

among the actionable dependencies. We further demonstrated that nucleotide depletion induces a replication stress overload with resultant lethal effect that is dependent upon endogenous MYC overexpression in human DLBCL cells. Our findings thus unravel a novel mechanism underlying MYC dysregulation in *ATM*-defective DLBCL, providing a therapeutic approach for MYC-driven DLBCL and potentially other high-grade B-NHL that exploits nucleotide biosynthesis as a liability conferred by MYC dysregulation.

Methods

Details of assays performed according to established protocols are shown in the *Online Supplementary Methods*.

Generation of *Atm*$^{-/-}$*nu*$^{-/-}$ mice

Animal studies were approved by the institutional ethics committee (AWERB) and conducted in accordance with UK Home Office regulations. The first mating of *Atm* heterozygote females (*Atm*$^{+/-}$*nu*$^{+/+}$; *129S6/SvEvTac-Atm*^{tm1Awb}*/J,* Jackson Laboratory, Maine, USA) with *Balb/c* nude males (*Atm*$^{+/+}$*nu*$^{-/-}$; Charles River, Harlow, UK) produced *Atm*$^{+/-}$*nu*$^{+/-}$ heterozygotes. Female *Atm*$^{+/-}$*nu*$^{+/-}$ progeny from the first generation underwent a second mating with male *Atm*$^{+/+}$*nu*$^{-/-}$ to obtain nude *Atm* heterozygotes (*Atm*$^{+/-}$*nu*$^{-/-}$). Finally, a third mating of second generation *Atm*$^{+/-}$*nu*$^{-/-}$ males with first generation *Atm*$^{+/-}$*nu*$^{+/-}$ females produced *Atm*$^{-/-}$*nu*$^{-/-}$ offspring.

Adoptive transfer of *Atm*$^{-/-}$nu$^{-/-}$ lymphomas and drug treatment

Lymphomas arising from *Atm*$^{-/-}$*nu*$^{-/-}$ mice (2x10^6 cells) were subcutaneously injected into NOD/LtSz-SCID/IL2γ^{tm1Wjl}/SzJ (NSG) mice (Charles River). Upon attaining average tumor volumes of 100mm^3/mouse, mice were randomized into 4 oral gavage treatment arms receiving mycophenolate mofetil (MMF, 100mg/kg/day; Selleckchem, Munich, Germany), adavosertib (AZD1775, 30mg/kg/day; AstraZeneca, Cambridge, UK), combined MMF and AZD1775, or vehicle; respectively. Animals were euthanized when tumor volume exceeded 1250mm^3.

Cell lines

Cell lines were established without Epstein-Barr virus infection, by culturing single-cell suspensions of *Atm*$^{-/-}$nu$^{-/-}$ lymphomas (1x10^6), in RPMI containing 15% FCS, 1% pyruvate,

1% NEAA/β-mercaptoethanol (50μM) and 1% penicillin/streptomycin (Life Technologies, Inchinnan, UK). Their immunophenotype and clonal relationship with the primary tumor were confirmed (Table S1).

Human and *Eμ-Myc* cell lines were cultured according to standard protocols (Supplementary Methods). Lymphoblastoid cell lines (LCL) were previously generated from samples obtained from A-T patients and healthy volunteers. Studies were approved by the West Midland, Coventry and Warwickshire Research Ethics Committee (REC: 20//WM/0098) and performed in accordance with local ethical guidelines. Written informed consent was obtained from all patients in accordance with the Declaration of Helsinki.

CRISPR/Cas9-mediated loss-of-function screen

Cell lines were modified to stably express *Cas9* and infected with the two-vector (lentiCas9-Blast and lentiGuide-Puro) lentiviral GeCKO v2.0 CRISPR knockout system (Addgene, MA) consisting of 130,209 pooled single-guide RNAs (sgRNA) targeting 20,661 genes and 1,000 control sgRNA. Cells were cultured at optimal cell number (1-6x10^8) to maintain ≥1000-fold coverage of the CRISPR sgRNA library. At day 0 and 18 (~14 doublings), DNA isolated from harvested viable cells was subjected to targeted deep sequencing of sgRNA using NextSeq HIGH 150 v2.5 kits on the NextSeq 500 sequencer (Illumina). The MAGeCK tool was used to determine sgRNA that were significantly depleted at day 18 compared to day 0 representing those targeting genes that were essential for cell survival ('hits').[19] KEGG pathway analysis was performed as for RNA-seq data.

Statistical analysis

Statistical analyses were performed using GraphPad Prism 9.2.0 (La Jolla, CA).

Results

***Atm*$^{-/-}$*nu*$^{-/-}$ mice develop B-cell lymphomas with complex karyotype that closely model human activated B-cell-like (ABC) and germinal center B-cell-like (GCB) DLBCL**

To model B-NHL that results from constitutional *ATM* loss, we generated a novel athymic *Atm*-deficient model (*Atm*$^{-/-}$*nu*$^{-/-}$) (Figure 1A). This overcomes an inherent limitation with *Atm*$^{-/-}$

mice which develop lethal thymoma in early life (<16 weeks) precluding their use to study B-cell lymphomagenesis.[20,21]

Crossing *Atm*$^{-/-}$ mice with *nu*$^{-/-}$ mice prevented thymoma development, leading to prolonged survival of *Atm*$^{-/-}$*nu*$^{-/-}$ mice, irrespective of whether death was caused by tumor or other causes, mostly infection (median survival 13 vs 23 weeks for *Atm*$^{-/-}$ vs *Atm*$^{-/-}$*nu*$^{-/-}$ mice) (Figure 1B; Figure S1). *Atm*$^{-/-}$*nu*$^{-/-}$ mice instead developed B-NHL, reminiscent of patients with A-T.[14,15] B-cell lymphomas emerged with 24% penetrance, manifesting in splenomegaly, frequent hepatomegaly and nodal involvement that arose at a median of 25 weeks (range 7-69) (Figure 1B). These lymphomas histologically and immunophenotypically resembled human DLBCL, with 6 of 14 lymphomas demonstrating Ki-67 >50%, and harboring identifiable clonal *IGHV-D-J* gene rearrangements (Figure 1C; Table S1).

B-cell lymphomagenesis in the context of constitutional *ATM* loss has also been recapitulated by the ATMKO.CD3εKO model generated by interbreeding *Atm*-deficient mice with CD3ε-knockout mice.[18] However, unlike the ATMKO.CD3εKO model wherein T-cell immunity is absent,[18] T-cells are present in the *Atm*$^{-/-}$*nu*$^{-/-}$ model, albeit at markedly reduced level (Figure 2A), akin to patients with A-T.[22] Early progenitor B-cell number retention ($B220^{+}CD43^{+}$) coupled with a trend towards reduced levels of more mature B-cell populations in the bone marrow (Figure 2A) and spleen (data not shown) in the *Atm*$^{-/-}$*nu*$^{-/-}$ model resembles A-T patients impaired B-cell development.[16] Moreover, in contrast to ATMKO.CD3εKO mice which were unable to form germinal centers and exclusively developed lymphomas resembling ABC DLBCL,[18] germinal centers were preserved in *Atm*$^{-/-}$*nu*$^{-/-}$ mice (Figure 2B). While the majority of *Atm*$^{-/-}$*nu*$^{-/-}$ lymphomas displayed gene expression signatures characteristic of human ABC DLBCL, some resembled GCB DLBCL (Figure 2C; Figure S2A,B).[23,24] *Atm*$^{-/-}$*nu*$^{-/-}$ mice therefore developed lymphomas that reflect the spectrum of DLBCL observed in patients harboring defective *ATM*.[9,13,24]

Atm$^{-/-}$*nu*$^{-/-}$ lymphomas exhibited a diverse landscape of complex karyotypic alterations (mean 10; range 5-17) indicating substantial intertumoral and intratumoral genetic heterogeneity (Figure 2D; Figure S2C). These alterations included chromosomal translocations and whole chromosome gains and losses, with the majority being subclonal. As found in human DLBCL,[25] *IgH* and *Myc* alterations were evident with *Myc* duplication present in 2 of 6 *Atm*$^{-/-}$*nu*$^{-/-}$ lymphomas (Figure S2C; Table S2). These features suggest a high level of genomic instability and clonal evolution in *Atm*$^{-/-}$*nu*$^{-/-}$ lymphomas likely driven in part by *Atm* loss. Taken together, our *Atm*$^{-/-}$*nu*$^{-/-}$ mice provide a robust model for the elucidation of pathogenic mechanisms and therapeutic targets in human DLBCL.

Atm$^{-/-}$*nu*$^{-/-}$ lymphomas are characterized by MYC activation

To decipher the biological processes underlying B-cell lymphomagenesis in *Atm*$^{-/-}$*nu*$^{-/-}$ mice, we characterized the transcriptomic landscape of *Atm*$^{-/-}$*nu*$^{-/-}$ lymphomas. RNA-seq data revealed 1493 upregulated and 1010 downregulated genes in *Atm*$^{-/-}$*nu*$^{-/-}$ lymphomas relative to healthy splenic B-cells from *Atm*$^{+/+}$*nu*$^{-/-}$ and *Atm*$^{+/-}$*nu*$^{-/-}$ mice (Figure 3A; Table S3).

Genes involved in cell cycle progression (e.g. *Ccnf*, *Cdk6*, *Ccnb1*, *Cdca5*), mitosis (e.g. *Klhl13*, *Psrc1, Spdl1, Kifc1),* DNA replication (e.g. *Orc1, Mcm6, Pole, Prim1, Rfc4*) and cellular metabolism (e.g. *Mgll, Gpt2, Uqcr10, Cox4i2*) were among the most significantly upregulated in *Atm*$^{-/-}$*nu*$^{-/-}$ lymphomas (Figure 3B; Table S4), reflecting the loss of ATM-dependent cell cycle checkpoints and resultant high proliferation rate. Concurrently, key genes mediating homologous recombination repair (e.g. *Rad51, Brca1, Pole)*, chromatin modification (e.g. *Ezh2, Cenpa*), replication stress response (e.g. *Wee1, Chk1*) and nucleotide biosynthesis (e.g. *Rrm2, Tyms)* were some of the most significantly overexpressed. Finally, reflecting the malignant properties of transformed B-cells in *Atm*$^{-/-}$*nu*$^{-/-}$ mice, tumor suppressor genes (e.g. *Txnip, Cul9*) and genes involved in normal B-cell development, signaling and activation (e.g. *Cr2*, *Akt3, Icosl, Cx3cr1)* as well as antigen presentation (e.g. *Cd1d1*) were significantly downregulated, whereas genes that promote tumor immune evasion (e.g. *Ctla4)* were upregulated (Tables S4 and 5).

An association between ATM loss, aberrant gene rearrangements and MYC deregulation has been previously established.[26] Moreover, ATM-dependent DNA damage response counteracts the tumorigenic effect of MYC activation, providing the basis for co-operation between ATM and MYC during tumorigenesis.[27-29] Concurring with this notion and the presence of *Myc* duplications in *Atm*$^{-/-}$*nu*$^{-/-}$ lymphomas, GSEA analysis of RNA-seq data demonstrated that MYC targets, and MYC-induced E2F targets, were among the most enriched gene sets in these lymphomas (Figure 3C,D; Figure S3A,B; Table S6), which was consistent with elevated MYC protein expression (Figure 3E; Figure S3C). As replication stress is a principal consequence of MYC dysregulation,[30] upregulation of replication stress response genes in *Atm*$^{-/-}$*nu*$^{-/-}$ lymphomas may be a consequence of upregulated MYC in the majority of these lymphomas. Other drivers, such as those involved in repair of DNA lesions induced by MYC-driven replication stress, may also play a role.[31] The transcriptomic landscape of *Atm*$^{-/-}$*nu*$^{-/-}$ lymphomas thus identified potentially targetable biological features, including DNA repair, a requirement for nucleotide biosynthesis due to replicative stress, and dysregulated MYC that likely underpin *ATM*-defective DLBCL oncogenesis (Figure 3F).[32-35]

Genome-wide CRISPR/Cas9 screen identifies nucleotide biosynthesis as a cellular dependency of *Atm*$^{-/-}$*nu*$^{-/-}$ lymphomas

We hypothesized that in a significant number of these lymphomas, heightened replication stress, due in part to MYC upregulation, could render these tumors dependent upon nucleotide biosynthesis. To systematically identify potentially actionable lymphoma-specific dependencies within our *Atm*$^{-/-}$*nu*$^{-/-}$ model, we performed a genome-scale CRISPR/Cas9-mediated loss-of-function screen on two *Atm*$^{-/-}$*nu*$^{-/-}$ lymphoma derived cell lines (50F2 and AN017) (Figure 4A).

At the optimal false discovery rate (FDR)-adjusted p-value threshold of 0.05 that produced a manageable gene output, 1000 and 340 hits were identified in 50F2 and AN017 respectively, with 197 hits common to both (Figure 4B,C; Table S7). Consistent with the observed MYC dysregulation, analysis of depleted sgRNA revealed a *Myc* dependency (rank 861; fold-change: -0.742) as well as dependency on key biological processes common to both cell lines (Figure 4D,E; Figure S4; Table S8). These included genes involved in DNA repair (e.g. *Parp1*, *Rad50, Rad51, Rnaseh2c, Mcm7*), DNA replication (e.g. *Pold2, Mcm7, Rnaseh2c*), telomere maintenance e.g. (*Pot1, Telo2*) and cell cycle regulation (e.g. *Cdk6*, *Fam58b)*, consistent with cellular dependence on alternative genome maintenance regulators upon *Atm* loss. Notably, the top hits identified from the CRISPR/Cas9 screen were also highly enriched in genes mediating nucleotide biosynthesis, including those encoding for the enzymes *Tyms, Umps, Cmpk1, Cad and Ppat* that play key roles in deoxynucleotide triphosphate (dNTP) production, as well as other important components within the purine biosynthesis pathway (Figure 4F,G). These observations therefore support the notion that both *Myc* activity and nucleotide biosynthesis are major cellular dependencies of *Atm*$^{-/-}$*nu*$^{-/-}$ lymphomas.

Nucleotide depletion induces replication stress overload and tumor-specific lethality in MYC-dependent *Atm*$^{-/-}$*nu*$^{-/-}$ lymphomas

The identification of MYC and nucleotide biosynthesis as cellular dependencies, together with evidence for their upregulation as part of a heightened replication stress response, raises the question of whether these lymphomas are sensitive to MYC inhibition and depletion of cellular nucleotide pools through inhibition of nucleotide biosynthesis. To address this, we examined the effect of MMF, an inhibitor of *de novo* purine biosynthesis,[36] on *Atm*$^{-/-}$*nu*$^{-/-}$ lymphomas. Moreover, since *Wee1* and *Rrm2* were among the most significantly overexpressed genes in *Atm*$^{-/-}$*nu*$^{-/-}$ lymphomas, we also evaluated the effect of

the WEE1 inhibitor, AZD1775, which can promote degradation of RRM2, a subunit of ribonucleotide reductase that is essential for dNTP biosynthesis.[37]

In vitro MYC inhibition of an *Atm*$^{-/-}$*nu*$^{-/-}$ lymphoma-derived cell line conferred significant cytotoxicity (Figure 5A). Furthermore, treatment of three *Atm*$^{-/-}$*nu*$^{-/-}$ lymphoma-derived cell lines with physiologically achievable concentrations of MMF or AZD1775 resulted in dose-dependent cytotoxicity, which was rescued via MYC inhibition (AZD) or addition of exogenous dNTP (MMF), consistent with the increased requirement for nucleotide biosynthesis caused by MYC activation (Figure 5B-D). Notably, MMF and AZD1775-induced cytotoxicity was also attained in *Atm* wild-type, *Eμ-Myc*-driven tumors that resemble human Burkitt lymphoma (Figure S5A).[38]

We reasoned that nucleotide depletion to catastrophic levels through concerted actions of MMF and AZD1775 in *Atm*$^{-/-}$*nu*$^{-/-}$ lymphomas might enhance lethality. Indeed, AZD1775 was synergistic when used in combination with MMF (Figure 5B,E), which was reversible upon MYC inhibition, dNTP supplementation or RRM2 upregulation via the specific NEDD8 inhibitor (NEDDi), pevonedistat (Figure 5C,D,F). As expected, AZD1775 treatment led to attenuated RRM2 levels in *Atm*$^{-/-}$*nu*$^{-/-}$ lymphoma cells and a derived-cell line (50F2) and activation of the replication stress response (Figure 5G; Figure S5B). The latter was evidenced by the induction of CHK1 phosphorylation, consistent with the exacerbation of replication stress upon nucleotide depletion.

To confirm the *in vivo* efficacy of nucleotide depletion as a therapeutic strategy, administration of MMF and AZD1775, alone or combined, to mice engrafted with an *Atm*$^{-/-}$*nu*$^{-/-}$ lymphoma (AT15c) was well-tolerated. Combined treatment significantly reduced tumor volume and delayed tumor growth as none of the tumors attained the maximum permitted tumor volume within this treatment group (Figure 5H).

The cytotoxicity of the nucleotide biosynthesis inhibitors was exerted via apoptosis (Figure 6A,B). This is likely due to replication stress overload as evidenced by impeded replication fork progression, resulting in fork stalling with compensatory initiation of nearby dormant origins upon combined MMF and AZD1775 treatment (Figure 6C).[39,40] The latter is supported by the retention of *Atm*$^{-/-}$*nu*$^{-/-}$ lymphoma cells in quiescent S-phase with the accumulation of partially-replicated DNA and lethal DNA damage (Figure 6D-F; Figure S5C).[41] Our observations in *Atm*$^{-/-}$*nu*$^{-/-}$ lymphomas therefore provided conceptual proof of nucleotide depletion as a viable therapeutic strategy for DLBCL harboring *MYC* dysregulation associated with *ATM* loss.

MYC overexpression broadly sensitizes human DLBCL cells to nucleotide depletion with AZD1775

Human DLBCL may exhibit *MYC* dysregulation concurrently with *ATM* disruption.[9] However, the majority of DLBCL with MYC overexpression do not exhibit *ATM* loss.[9,13,42] To determine whether the use of nucleotide depletion as a therapeutic strategy can be broadly extended to human DLBCL harboring *MYC* dysregulation associated with pathogenic mechanisms beyond *ATM* loss, we set out to validate such a therapeutic strategy within these contexts.

Human DLBCL cell lines were sensitive to MYC inhibition and physiologically achievable doses of MMF and AZD1775, which for AZD1775, correlated with MYC upregulation (Figure 7A-C; Figure S3C; Figure S6A,B). Similar to *Atm*$^{-/-}$*nu*$^{-/-}$ lymphomas, synergism was evident upon AZD1775 and MMF co-treatment particularly in high MYC-expressing cell lines (Figure 7C,D; Figure S6A), with MYC inhibition reducing cytotoxicity (Figure 7E). In contrast, loss of ATM did not impact upon MMF or AZD1775 sensitivity in A-T patient-derived LCL cells nor in CLL-derived CII cells with ATM knockdown (Figure S6C,D). Moreover, the ATM-deficient DLBCL cell line (Farage) was AZD1775-resistant (Figure 7C; Figure S6A,E). Upon mining the Cancer Dependency Map (DepMap)[43] data that uncovers gene dependencies in hundreds of cancer cell lines we observed a significant inverse correlation between protein expression of two nucleotide biosynthesis genes (CAD, UMPS) and MYC, but not ATM (Figure 7F). In addition, mining published human DLBCL RNA-seq datasets revealed that, compared to germinal center B-cells, ABC DLBCL concurrently express significantly reduced *ATM* and elevated *MYC* levels. Furthermore, *MYC* expression is higher in the ABC than the GCB DLBCL cohort whilst expression of a purine/pyrimidine biosynthesis gene-set is elevated in ABC DLBCL in comparison to both GCB DLBCL and germinal center B-cells (Figure S6F). Thus, nucleotide biosynthesis inhibition may be particularly relevant for an ABC DLBCL subgroup characterized by upregulated MYC. Consistent with this notion, a high-MYC expressing human Burkitt lymphoma cell line was more sensitive to nucleotide biosynthesis inhibition than a low-MYC expressing cell line (Figure S7).

Akin to *Atm*$^{-/-}$*nu*$^{-/-}$ lymphoma cells, cytotoxicity of these nucleotide biosynthesis inhibitors was exerted via apoptosis in high MYC-expressing human DLBCL (OC-ILY3) (Figure 8A,B), likely due to exacerbation of replication stress as evidenced by retention of cells in quiescent S-phase and activation of the replication stress response (Figure 8C-E).

Taken together, these results show that response to nucleotide depletion in human lymphoma is influenced by MYC expression rather than *ATM* mutation status, thus

demonstrating its broad applicability as a therapeutic approach independent of the mechanism underlying MYC dysregulation. Also, whilst the *Atm*$^{-/-}$*nu*$^{-/-}$ lymphomas and derived cell lines provide a model for DLBCL developed by A-T patients this could potentially also be useful for patients with high MYC-expressing DLBCL without A-T.

Discussion

High-grade B-NHL is the commonest tumor type in patients with ataxia-telangiectasia, representing 37%-53% of cancer diagnoses in these individuals.[14,15] However, only a proportion of A-T patients develop tumors,[14] and the mechanisms of B-cell tumorigenesis underlying *ATM* loss remains unresolved. Moreover, the use of chemoradiotherapy for lymphoma treatment can be especially toxic for these patients owing to their inherent cellular chemoradiosensitivity.[14] Hence, the identification of therapeutic targets and development of alternative cancer treatments represents a critical unmet need.

In this context, our *Atm*$^{-/-}$*nu*$^{-/-}$ murine model closely recapitulates conditions under which lymphomagenesis occurs in human A-T including thymic aplasia and retention of a low-level of T-cells arrested at the $CD3^+CD8^+$ and $CD3^+CD4^+$ differentiation stage.[22] Importantly, *Atm*$^{-/-}$ *nu*$^{-/-}$ mice retained germinal centers and developed GCB as well as ABC DLBCL, reminiscent of the phenotypic spectrum in ATM-defective human DLBCL.[9] To enable unbiased discovery of additional pathogenic processes and targetable lymphoma addictions, we systematically interrogated our *Atm*$^{-/-}$*nu*$^{-/-}$ model with genome-scale technology incorporating RNA-seq and CRISPR/Cas9 loss-of-function screens, approaches that have not previously been utilized to study ATM-defective DLBCL.

Our analysis uncovered a MYC-driven lymphoproliferation occurring in the context of constitutional *ATM* loss that characterizes A-T. However, whilst ATM inactivation initiates the genesis of *Atm*$^{-/-}$*nu*$^{-/-}$ lymphomas, it remains unclear whether ATM deficiency is an ongoing dependency in these tumors. Furthermore, well-known genetic mechanisms involving chromosomal rearrangements or gene amplifications only give rise to ~35% of MYC overexpressing high-grade B-NHL.[3-5,25] Likewise, genetic disruptions involving *Myc* were observed in some *Atm*$^{-/-}$*nu*$^{-/-}$ lymphomas but were absent in other instances of MYC dysregulation. Thus, future studies are required to determine the long-term effect of ATM deficiency on lymphomagenesis and the mechanisms that contribute to MYC activation in this murine model.

Our analysis revealed actionable dependencies beyond B-cell receptor signaling in *ATM*-defective DLBCL. In fact, from our CRISPR/Cas9 screens we observed dependency on key B-cell receptor signaling genes in only one of two evaluated *Atm*$^{-/-}$*nu*$^{-/-}$ lymphoma cell lines (50F2). On the contrary, nucleotide biosynthesis emerged as one of the most prominent dependencies in both lymphoma lines, alongside DNA repair, DNA replication and cell cycle regulation, which were also significantly upregulated processes in our RNA-seq dataset. We showed that nucleotide metabolism in the context of *Atm* loss is a MYC-dependent vulnerability, which can be effectively targeted by nucleotide depletion through the synergistic actions of MMF and AZD1775. Our findings are consistent with a mechanistic model in which MYC induces replication stress by multiple transcription-dependent[44] and transcription-independent mechanisms.[31,45] Moderate levels of replication stress support tumor progression via generation of genomic instability whilst excessive levels are prevented by MYC-regulated nucleotide biosynthesis that becomes essential for tumor survival.[46] Combining MMF and AZD1775 potently inhibits nucleotide biosynthesis, leading to depletion of cellular dNTP that exacerbates replication stress. In turn, the accumulation of replication stress to catastrophic levels results in lymphoma lethality (Figure 8F). It remains to be determined whether other causes of replication stress or different mechanisms can render lymphoma cells dependent on nucleotide biosynthesis in the absence of MYC upregulation, as observed in two DLBCL cell lines with low MYC expression.

Targeted therapies, such as ibrutinib, have been associated with disappointing responses[47] coupled with possible enrichment of cells overexpressing MYC targets in ibrutinib-resistant DLBCL.[48] We confirmed the broad applicability of nucleotide depletion as a therapeutic strategy for MYC-driven DLBCL independent of *ATM* status in human DLBCL models. In this regard, a previous study showed that inhibition of phosphoribosyl pyrophosphate synthetase 2, an enzyme essential for purine biosynthesis, is synthetically lethal in MYC-driven murine lymphoma.[49] Herein, we demonstrated a complementary strategy to inhibit nucleotide biosynthesis in DLBCL through synthetic lethality between RRM2 depletion and MYC overexpression, which is potentiated in the presence of MMF (Figure 8F). We showed that depletion of RRM2, a ribonucleotide reductase subunit essential for nucleotide biosynthesis, can be achieved through AZD1775, the WEE1 inhibitor under active clinical investigation in DLBCL (NCT02465060, NCT04439227). Indeed, a recent study demonstrating selectivity of AZD1775 monotherapy against MYC-overexpressing DLBCL[41] lends further support to a synthetically lethal interaction between MYC overexpression and RRM2 loss. While clinical trials in solid tumors showed AZD1775 to be generally well-tolerated,[50-52] our findings support the clinical evaluation of the AZD1775-MMF combination in DLBCL, including among ataxia-telangiectasia patients. Our results also support the investigation of MYC

overexpression as a predictive biomarker of response to inform patient selection into these trials.

Finally, our CRISPR/Cas9 screen identified other core components within the purine or pyrimidine biosynthetic pathway that could serve as synthetically lethal partners with MYC overexpression and/or *ATM* loss, and therefore deserve further investigation as therapeutic targets. These include phosphoribosyl pyrophosphate amidotransferase (PPAT), carbamoyl-phosphate synthetase (CAD), thymidylate synthetase (TYMS) and uridine 5'-monophosphate synthase (UMPS). Collectively, our findings highlight nucleotide metabolism as a compelling therapeutic vulnerability with potential for further development into a novel treatment paradigm for clinically high-risk, MYC-driven lymphoma. This approach is garnering interest in haemato-oncology with a dihydroorotate dehydrogenase inhibitor (BAY2402234) already in a phase I clinical trial for myeloid malignancies.[53,54]

References

1. Ott G, Rosenwald A, Campo E. Understanding MYC-driven aggressive B-cell lymphomas: pathogenesis and classification. Blood. 2013;122(24):3884-3891.

2. Sehn LH, Salles G. Diffuse Large B-Cell Lymphoma. N Engl J Med. 2021;384(9):842-858.

3. Copie-Bergman C, Cuilliere-Dartigues P, Baia M, et al. MYC-IG rearrangements are negative predictors of survival in DLBCL patients treated with immunochemotherapy: a GELA/LYSA study. Blood. 2015;126(22):2466-2474.

4. Horn H, Ziepert M, Becher C, et al. MYC status in concert with BCL2 and BCL6 expression predicts outcome in diffuse large B-cell lymphoma. Blood. 2013;121(12):2253-2263.

5. Staiger AM, Ziepert M, Horn H, et al. Clinical Impact of the Cell-of-Origin Classification and the MYC/ BCL2 Dual Expresser Status in Diffuse Large B-Cell Lymphoma Treated Within Prospective Clinical Trials of the German High-Grade Non-Hodgkin's Lymphoma Study Group. J Clin Oncol. 2017;35(22):2515-2526.

6. Scott DW, King RL, Staiger AM, et al. High-grade B-cell lymphoma with MYC and BCL2 and/or BCL6 rearrangements with diffuse large B-cell lymphoma morphology. Blood. 2018;131(18):2060-2064.

7. Rosenwald A, Bens S, Advani R, et al. Prognostic Significance of MYC Rearrangement and Translocation Partner in Diffuse Large B-Cell Lymphoma: A Study by the Lunenburg Lymphoma Biomarker Consortium. J Clin Oncol. 2019;37(35):3359-3368.

8. Petrich AM, Gandhi M, Jovanovic B, et al. Impact of induction regimen and stem cell transplantation on outcomes in double-hit lymphoma: a multicenter retrospective analysis. Blood. 2014;124(15):2354-2361.

9. Reddy A, Zhang J, Davis NS, et al. Genetic and Functional Drivers of Diffuse Large B Cell Lymphoma. Cell. 2017;171(2):481-494.e15.

10. Melchardt T, Hufnagl C, Weinstock DM, et al. Clonal evolution in relapsed and refractory diffuse large B-cell lymphoma is characterized by high dynamics of subclones. Oncotarget. 2016;7(32):51494-51502.

11. Leeksma OC, de Miranda NF, Veelken H. Germline mutations predisposing to diffuse large B-cell lymphoma. Blood Cancer J. 2017;7(2):e532.

12. Grønbaek K, Worm J, Ralfkiaer E, Ahrenkiel V, Hokland P, Guldberg P. ATM mutations are associated with inactivation of the ARF-TP53 tumor suppressor pathway in diffuse large B-cell lymphoma. Blood. 2002;100(4):1430-1437.

13. Xu-Monette ZY, Zhang H, Zhu F, et al. A refined cell-of-origin classifier with targeted NGS and artificial intelligence shows robust predictive value in DLBCL. Blood Adv. 2020;4(14):3391-3404.

14. Suarez F, Mahlaoui N, Canioni D, et al. Incidence, presentation, and prognosis of malignancies in ataxia-telangiectasia: a report from the French national registry of primary immune deficiencies. J Clin Oncol. 2015;33(2):202-208.

15. Bakhtiar S, Salzmann-Manrique E, Donath H, et al. The incidence and type of cancer in patients with ataxia-telangiectasia via a retrospective single-centre study. Br J Haematol. 2021;194(5):879-887.

16. Rothblum-Oviatt C, Wright J, Lefton-Greif MA, McGrath-Morrow SA, Crawford TO, Lederman HM. Ataxia telangiectasia: a review. Orphanet J Rare Dis. 2016;11(1):159.

17. Lee JH, Paull TT. Cellular functions of the protein kinase ATM and their relevance to human disease. Nat Rev Mol Cell Biol. 2021;22(12):796-814.

18. Hathcock KS, Padilla-Nash HM, Camps J, et al. ATM deficiency promotes development of murine B-cell lymphomas that resemble diffuse large B-cell lymphoma in humans. Blood. 2015;126(20):2291-2301.

19. Li W, Xu H, Xiao T, et al. MAGeCK enables robust identification of essential genes from genome-scale CRISPR/Cas9 knockout screens. Genome Biol. 2014;15(12):554.

20. Barlow C, Hirotsune S, Paylor R, et al. Atm-deficient mice: a paradigm of ataxia telangiectasia. Cell. 1996;86(1):159-171.

21. Xu Y, Ashley T, Brainerd EE, Bronson RT, Meyn MS, Baltimore D. Targeted disruption of ATM leads to growth retardation, chromosomal fragmentation during meiosis, immune defects, and thymic lymphoma. Genes Dev. 1996;10(19):2411-2422.

22. Chopra C, Davies G, Taylor M, et al. Immune deficiency in Ataxia-Telangiectasia: a longitudinal study of 44 patients. Clin Exp Immunol. 2014;176(2):275-282.

23. Alizadeh AA, Eisen MB, Davis RE, et al. Distinct types of diffuse large B-cell lymphoma identified by gene expression profiling. Nature. 2000;403(6769):503-511.

24. Wright G, Tan B, Rosenwald A, Hurt EH, Wiestner A, Staudt LM. A gene expression-based method to diagnose clinically distinct subgroups of diffuse large B cell lymphoma. Proc Natl Acad Sci U S A. 2003;100(17):9991-9996.

25. Pophali PA, Marinelli LM, Ketterling RP, et al. High level MYC amplification in B-cell lymphomas: is it a marker of aggressive disease? Blood Cancer J. 2020;10(1):5.

26. Liyanage M, Weaver Z, Barlow C, et al. Abnormal rearrangement within the alpha/delta T-cell receptor locus in lymphomas from Atm-deficient mice. Blood. 2000;96(5):1940-1946.

27. Maclean KH, Kastan MB, Cleveland JL. Atm deficiency affects both apoptosis and proliferation to augment Myc-induced lymphomagenesis. Mol Cancer Res. 2007;5(7):705-711.

28. Shreeram S, Hee WK, Demidov ON, et al. Regulation of ATM/p53-dependent suppression of myc-induced lymphomas by Wip1 phosphatase. J Exp Med. 2006;203(13):2793-2799.

29. Pusapati RV, Rounbehler RJ, Hong S, et al. ATM promotes apoptosis and suppresses tumorigenesis in response to Myc. Proc Natl Acad Sci U S A. 2006;103(5):1446-1451.

30. Curti L, Campaner S. MYC-Induced Replicative Stress: A Double-Edged Sword for Cancer Development and Treatment. Int J Mol Sci. 2021;22(12):6168.

31. Dominguez-Sola D, Ying CY, Grandori C, et al. Non-transcriptional control of DNA replication by c-Myc. Nature. 2007;448(7152):445-451.

32. Bester AC, Roniger M, Oren YS, et al. Nucleotide deficiency promotes genomic instability in early stages of cancer development. Cell. 2011;145(3):435-446.

33. Hastak K, Paul RK, Agarwal MK, et al. DNA synthesis from unbalanced nucleotide pools causes limited DNA damage that triggers ATR-CHK1-dependent p53 activation. Proc Natl Acad Sci U S A. 2008;105(17):6314-6319.

34. Poli J, Tsaponina O, Crabbe L, et al. dNTP pools determine fork progression and origin usage under replication stress. EMBO J. 2012;31(4):883-894.

35. Zeman MK, Cimprich KA. Causes and consequences of replication stress. Nat Cell Biol. 2014;16(1):2-9.

36. Allison AC, Eugui EM. Mycophenolate mofetil and its mechanisms of action. Immunopharmacology. 2000;47(2-3):85-118.

37. Pfister SX, Markkanen E, Jiang Y, et al. Inhibiting WEE1 Selectively Kills Histone H3K36me3-Deficient Cancers by dNTP Starvation. Cancer Cell. 2015;28(5):557-568.

38. Adams JM, Harris AW, Pinkert CA, et al. The c-myc oncogene driven by immunoglobulin enhancers induces lymphoid malignancy in transgenic mice. Nature. 1985;318(6046):533-538.

39. Ge XQ, Jackson DA, Blow JJ. Dormant origins licensed by excess Mcm2-7 are required for human cells to survive replicative stress. Genes Dev. 2007;21(24):3331-3341.

40. Ibarra A, Schwob E, Mendez J. Excess MCM proteins protect human cells from replicative stress by licensing backup origins of replication. Proc Natl Acad Sci U S A. 2008;105(26):8956-8961.

41. Young LA, O'Connor LO, de Renty C, et al. Differential Activity of ATR and WEE1 Inhibitors in a Highly Sensitive Subpopulation of DLBCL Linked to Replication Stress. Cancer Res. 2019;79(14):3762-3775.

42. Schmitz R, Wright GW, Huang DW, et al. Genetics and Pathogenesis of Diffuse Large B-Cell Lymphoma. N Engl J Med. 2018;378(15):1396-1407.

43. Tsherniak A, Vazquez F, Montgomery PG, et al. Defining a Cancer Dependency Map. Cell. 2017;170(3):564-576.e516.

44. Lin CY, Loven J, Rahl PB, et al. Transcriptional amplification in tumor cells with elevated c-Myc. Cell. 2012;151(1):56-67.

45. Macheret M, Halazonetis TD. Intragenic origins due to short G1 phases underlie oncogene-induced DNA replication stress. Nature. 2018;555(7694):112-116.

46. Liu YC, Li F, Handler J, et al. Global regulation of nucleotide biosynthetic genes by c-Myc. PLoS One. 2008;3(7):e2722.

47. Wilson WH, Young RM, Schmitz R, et al. Targeting B cell receptor signaling with ibrutinib in diffuse large B cell lymphoma. Nat Med. 2015;21(8):922-926.

48. Shaffer AL, 3rd, Phelan JD, Wang JQ, et al. Overcoming Acquired Epigenetic Resistance to BTK Inhibitors. Blood Cancer Discov. 2021;2(6):630-647.

49. Cunningham JT, Moreno MV, Lodi A, Ronen SM, Ruggero D. Protein and nucleotide biosynthesis are coupled by a single rate-limiting enzyme, PRPS2, to drive cancer. Cell. 2014;157(5):1088-1103.

50. Do K, Wilsker D, Ji J, et al. Phase I Study of Single-Agent AZD1775 (MK-1775), a Wee1 Kinase Inhibitor, in Patients With Refractory Solid Tumors. J Clin Oncol. 2015;33(30):3409-3415.

51. Liu JF, Xiong N, Campos SM, et al. Phase II Study of the WEE1 Inhibitor Adavosertib in Recurrent Uterine Serous Carcinoma. J Clin Oncol. 2021;39(14):1531-1539.

52. Seligmann JF, Fisher DJ, Brown LC, et al. Inhibition of WEE1 Is Effective in TP53- and RAS-Mutant Metastatic Colorectal Cancer: A Randomized Trial (FOCUS4-C) Comparing Adavosertib (AZD1775) With Active Monitoring. J Clin Oncol. 2021;39(33):3705-3715.

53. Christian S, Merz C, Evans L, et al. The novel dihydroorotate dehydrogenase (DHODH) inhibitor BAY 2402234 triggers differentiation and is effective in the treatment of myeloid malignancies. Leukemia. 2019;33(10):2403-2415.

54. Sexauer AN, Alexe G, Gustafsson K, et al. DHODH: A promising target in the treatment of T-Acute Lymphoblastic Leukemia. Blood Adv. 2023;7(21):6685-6701.

55. Morin RD, Johnson NA, Severson TM, et al. Somatic mutations altering EZH2 (Tyr641) in follicular and diffuse large B-cell lymphomas of germinal-center origin. Nat Genet. 2010;42(2):181-185.

56. Beguelin W, Popovic R, Teater M, et al. EZH2 is required for germinal center formation and somatic EZH2 mutations promote lymphoid transformation. Cancer Cell. 2013;23(5):677-692.

57. Liberzon A, Birger C, Thorvaldsdottir H, Ghandi M, Mesirov JP, Tamayo P. The Molecular Signatures Database (MSigDB) hallmark gene set collection. Cell Syst. 2015;1(6):417-425.

Figure legends.

Figure 1. *Atm*$^{-/-}$*nu*$^{-/-}$ mice develop B-cell lymphomas that resemble human diffuse large B-cell lymphoma (DLBCL). (A) Schematic diagram summarizing experimental studies to characterize the *Atm*$^{-/-}$*nu*$^{-/-}$ murine model with the aim to identify therapeutic targets that can be translated to human B-cell non-Hodgkin lymphoma (B-NHL). (B) Kaplan-Meier curves displaying prolonged overall survival of *Atm*$^{-/-}$*nu*$^{-/-}$ (n=97) and *Atm*$^{+/+}$*nu*$^{-/-}$ (n=17) mice in comparison to *Atm*$^{-/-}$*nu*$^{+/-}$ (n=23) and *Atm*$^{-/-}$*nu*$^{+/+}$ (n=13) mice ($P \leq 0.0001$). Inset: *Atm*$^{-/-}$*nu*$^{-/-}$ littermates (7-69 wks old) had enlarged spleens and livers in comparison to their *Atm*$^{+/+}$*nu*$^{+/+}$ and *Atm*$^{+/+}$*nu*$^{-/-}$ counterparts. (C) Immunohistology and morphology indicates that tumors from *Atm*$^{-/-}$*nu*$^{-/-}$ mice are lymphomas of B-cell origin resembling human DLBCL. Representative images of sections (original magnification x10 and insets x40) from two representative *Atm*$^{-/-}$*nu*$^{-/-}$ DLBCL (5F1, 519) stained with haematoxylin/eosin (H&E) as well as for B-cell (CD10, CD20, B220), T-cell (CD3), proliferation (Ki67, CD10) and DLBCL (PAX5, IRF4, FOXP1, CD10) markers are depicted.

Figure 2. B-cell lymphomas that develop in *Atm*$^{-/-}$*nu*$^{-/-}$ mice have a complex karyotype that resembles human activated B-cell-like (ABC) and germinal center B-cell-like (GCB) diffuse large B-cell lymphoma (DLBCL). (A) FACS analysis of splenic T-cell and bone marrow B-cell populations of 6-8 week old mice revealed reduced but not completely absent T-cell populations in *Atm*$^{+/+}$*nu*$^{-/-}$ (n=4) and *Atm*$^{-/-}$*nu*$^{-/-}$ (n=5) mice compared to *Atm*$^{+/+}$*nu*$^{+/+}$ (n=16), *Atm*$^{-/-}$*nu*$^{+/+}$ (n=19) and *Atm*$^{+/+}$*nu*$^{+/-}$ (n=6). T-cells were arrested at the CD3^{+}CD8^{+} and CD3^{+}CD4^{+} differentiation stage. Significantly fewer precursor (B220^{+}CD43^{-}) and transitional (B220^{high}CD43^{-}IgM^{+}) B-cells were evident in the bone marrow of *Atm*$^{-/-}$*nu*$^{-/-}$ mice compared to their *Atm*$^{+/+}$*nu*$^{+/+}$ and/or *Atm*$^{-/-}$*nu*$^{+/+}$ counterparts, whilst the levels of progenitor (B220^{+}CD43^{+}) B-cells were similar across all genotypes. Immature (B220^{med}CD43^{-}IgM^{+}) B-cell levels were highly variable even within genotypes. Data are presented as mean ± SEM. Statistical significance, ascertained by one-way ANOVA with Tukey post-hoc test, is denoted by: *$P \leq 0.05$, **$P \leq 0.01$, ***$P \leq 0.005$, ****$P \leq 0.001$, *****$P \leq 0.0005$, ******$P \leq 0.0001$. (B) Germinal centers (arrows); albeit with perturbed morphology and larger than normal; were evident in various lymph nodes (LN) and gut mucosa of *Atm*$^{-/-}$*nu*$^{-/-}$ mice. Representative images of sections (original magnification: x5, pancreas; x10, neck, intestine) stained with H&E are depicted. (C) Comparison of ribonucleic acid (RNA)-seq data of *Atm*$^{-/-}$*nu*$^{-/-}$ lymphomas (n=11) and control splenic B-cells from *Atm*$^{+/+}$*nu*$^{-/-}$ and *Atm*$^{+/-}$*nu*$^{-/-}$ mice (n=2) against published RNA-seq datasets of human ABC DLBCL and healthy control germinal center (GC) B-cells[55,56] suggests that the majority of *Atm*$^{-/-}$*nu*$^{-/-}$ lymphomas cluster with human ABC DLBCL.[9] (D) Left panel: Specific translocations involving *IgH* and *Myc* were assessed by M-Fluorescence in situ hybridization

(FISH) in six *Atm*$^{-/-}$*nu*$^{-/-}$ lymphomas. The representative example shown (5F3) harbored *Myc* gain and *IgH* loss as indicated by the arrows *(IgHa*, red; *IgHVi*, green; *Myc*, red). Right panel: The circos plot summarizing the chromosomal alterations for the 6 *Atm*$^{-/-}$*nu*$^{-/-}$ B-cell lymphoma revealed an absence of common translocations. Chromosomes are indicated by the numerals and annotated with lymphoma relevant genes localized in the regions affected by chromosomal alterations.

Figure 3. *Atm*$^{-/-}$*nu*$^{-/-}$ lymphomas display a transcriptional profile characterized by MYC activation. (A) RNA-seq analysis of *Atm*$^{-/-}$*nu*$^{-/-}$ lymphomas (n=11) and control splenic B-cells from *Atm*$^{+/+}$*nu*$^{-/-}$ and *Atm*$^{+/-}$*nu*$^{-/-}$ mice (n=2) revealed differentially expressed genes in *Atm*$^{-/-}$*nu*$^{-/-}$ lymphomas; 1493 upregulated (red) and 1010 downregulated (blue). (B,C) Biological processes that are the most significantly upregulated in *Atm*$^{-/-}$*nu*$^{-/-}$ lymphomas compared to control splenic B-cells as revealed by (B) Kyoto Encyclopaedia of Genes and Genomes (KEGG) pathway and (C) Gene Set Enrichment Analysis (GSEA) hallmark pathway analyses. (D) Comparison of the murine RNA-seq data to human ABC (n=252), GCB (n=278) and unknown (n=94) DLBCL;[9] stratified according to MYC target gene expression: MYC high (n=201) and low (n=436)[57] reveals that a high proportion of *Atm*$^{-/-}$*nu*$^{-/-}$ lymphomas align with high MYC-expressing human DLBCL. (E) MYC expression is upregulated in the majority of *Atm*$^{-/-}$*nu*$^{-/-}$ lymphomas (5F3, 50F2, 703, AN017, AN009) in comparison to murine basal controls: M3$^{+/+}$ (*Atm*$^{+/+}$*nu*$^{+/+}$), Nu$^{-/-}$(*Atm*$^{+/+}$*nu*$^{-/-}$), F2$^{-/+}$ (*Atm*$^{-/+}$*nu*$^{+/+}$); MYC positive control: L41F1$^{-/-}$(*Atm*$^{-/-}$*nu*$^{+/+}$); and also human ATM isogenic CII CLL cell lines, LCLs derived from healthy and ataxia-telangiectasia (A-T) individuals with WILL-2 (human DLBCL) as a MYC positive control on a separate gel. (F) Summary of the most relevant significantly upregulated (red) and downregulated (blue) genes and biological processes in *Atm*$^{-/-}$*nu*$^{-/-}$ lymphomas.

Figure 4. Genome-wide CRISPR/Cas9 screen identifies nucleotide biosynthesis as a cellular dependency of *Atm*$^{-/-}$*nu*$^{-/-}$ lymphomas. (A) Identification of cellular dependencies by genome-scale clustered regularly interspaced short palindromic repeats (CRISPR)/Cas9-mediated loss-of-function screens of two cell lines established from *Atm*$^{-/-}$*nu*$^{-/-}$ lymphomas (50F2 and AN017). (B) Cumulative number of hits (from 21513 potential genes) at various false discovery rates (FDR) in each individual cell line and common to both (combined). A 5% FDR (FDR <0.05) was set for all further analysis. (C) The number of mutually exclusive and common hits between the two cell lines at FDR <0.05. (D) Major biological processes represented by the discovered hits from the CRISPR/Cas9 screen. These processes were also upregulated in *Atm*$^{-/-}$*nu*$^{-/-}$ lymphomas as evidenced from RNA-seq data. (E) KEGG pathway analysis of hits common to both *Atm*$^{-/-}$*nu*$^{-/-}$ lymphoma cell lines revealing essential

cellular dependencies. (F,G) Hits identified within the purine biosynthesis pathway (dark orange), the most significantly affected biological process, that represent potential therapeutic targets.

Figure 5. Nucleotide depletion induces replication stress overload and lethality in MYC-dependent *Atm*$^{-/-}$*nu*$^{-/-}$ lymphomas. (A) Exposure for 72h, of the *Atm*$^{-/-}$*nu*$^{-/-}$ lymphoma cell line, 50F2, to a MYC inhibitor (MYCi, MYCi361); at doses reported (Selleckchem) to specifically inhibit MYC activity; led to significant toxicity as measured by CellTitre-Glo assay. (B-D) Exposure of *Atm*$^{-/-}$*nu*$^{-/-}$ lymphoma cell lines (703, 5F3, 50F2) to mycophenolate mofetil (MMF) and/or adavosertib (AZD1775) for 72h led to significant toxicity as measured by (B) Alamar Blue, (C) CellTitre-Glo or (D) Propidium Iodide (PI) exclusion that could be rescued by (C) inhibition of MYC or (D) addition of exogenous nucleosides. (C) Surviving fraction was normalized to the appropriate MYCi dose to highlight any rescue from MMF and/or AZD1775 toxicity. (E) Combining MMF and AZD1775 results in synergistic cytotoxicity. (F) The cytotoxic effect of MMF and AZD1775 can be ameliorated by upregulation of RRM2 via NEDD8 inhibition (MLN4924, pevonedistat). (C,D,F) Cell lines were treated with MMF doses corresponding to the EC_{50} and 400nM AZD1775. (G) AZD1775 (400nM; 72h) exerts its effects via depletion of RRM2 and subsequent exacerbation of replication stress, on an *Atm*-deficient background, via reduction of ATR-mediated deoxyribonucleic acid (DNA) repair activity in *Atm*$^{-/-}$*nu*$^{-/-}$ lymphoma cell lines. Irradiated (IR, 6Gy, 30min) A-T patient-derived LCLs serve as a positive control. (H) Nucleotide depletion with AZD1775 and MMF demonstrated significant activity *in vivo*. NSG mice harboring adoptively transferred *Atm*$^{-/-}$*nu*$^{-/-}$ lymphoma (AT15c) were administered vehicle (n=4), MMF (100mg/kg; n=5), AZD1775 (30mg/kg; n=5), or a combination of MMF and AZD1775 (n=6) via oral gavage for 7 days. Overall tumor size was significantly smaller in animals receiving combination therapy, in comparison to AZD1775 alone. Data are presented as mean ± SEM of (A,C) 50F2, (B,D,F) the three cell lines (703, 5F3, 50F2) or (H) mice per treatment arm. All cytotoxicity experiments were performed at least in quadruplicate. Statistical significance versus Vehicle (*), MMF (†), AZD1775 (+), MYCi, nucleoside or NEDDi (‡), was ascertained by matched multi-comparison (A) one-way or (B,C,D,F,H) two-way ANOVA with Tukey post-hoc test denoted by: *P≤0.05, **P≤0.01, ***P≤0.005, ****P≤0.001, *****P≤0.0005, ******P≤0.0001.

Figure 6. Nucleotide depletion induces replication stress-mediated apoptosis in *Atm*$^{-/-}$ *nu*$^{-/-}$ lymphomas. (A,B) Exposure (72h) of *Atm*$^{-/-}$*nu*$^{-/-}$ lymphoma cell lines (703, 5F3, 50F2) to vehicle, MMF (250nM) or AZD1775 (400nM), alone or in combination, led to cell death primarily via apoptosis. (A) Apoptosis was distinguished from mitotic catastrophe by 4',6-

diamidino-2-phenylindole (DAPI)$^{+}$/Lamin B^{-}/phospho (p)-Histone H3-S10^{-} immunofluorescence staining in the former, and DAPI^{+}/Lamin B^{+}/p-Histone H3-S10^{-} staining in the latter. (B) Apoptosis was confirmed by Annexin V (AxV)/PI status: viable (AxV^{-}/PI^{-}), early apoptotic (AxV^{+}/PI^{-}), late apoptotic (AxV^{+}/PI^{+}), secondary necrotic (AxV^{-}/PI^{+}). (C) Replication fork progression in *Atm*$^{-/-}$*nu*$^{-/-}$ lymphomas measured by DNA fibre analysis; was significantly impeded by combination treatment with AZD1775 and MMF. (D) Cell cycle profiles of an *Atm*$^{-/-}$*nu*$^{-/-}$ lymphoma (50F2, n=3) showed an accumulation of tumor cells in S-phase upon combination treatment with AZD1775 and MMF. (E) Replicating (active, EDU^{+}) and non-replicating (inactive, EDU^{-}) cells in S-phase were distinguished by EDU positivity. In an *Atm*$^{-/-}$*nu*$^{-/-}$ lymphoma (50F2, n=3), combined treatment with AZD1775 and MMF led to accumulation of non-replicating cells residing in S-phase. (F) The proportion of γH2AX^{+} cells in non-replicating (inactive, EDU^{-}) S-phase was determined by flow cytometry. Combined treatment with AZD1775 and MMF resulted in γH2AX accumulation in *Atm*$^{-/-}$*nu*$^{-/-}$ lymphoma cells (50F2, n=3). Data are presented as mean ± SEM of (A-C) the three cell lines (703, 5F3, 50F2) or (D-F) 50F2. All experiments were performed at least in triplicate. Statistical significance ascertained by (A-E) matched multi-comparison two-way ANOVA with Tukey post-hoc test and (F) repeat-measures matched multi-comparison one-way ANOVA with Tukey post-hoc test denoted by: *P≤0.05, **P≤0.01, ***P≤0.005, ****P≤0.001, *****P≤0.0005, ******P≤0.0001. (B) Statistical significance of Viable (*), Early Apoptotic (†), Late Apoptotic (+), or Necrotic (‡) cells. (E) Inactive cell comparison (+).

Figure 7. High MYC expression sensitizes human DLBCL cells to AZD1775 induced nucleotide depletion. (A) Exposure of OCI-LY3, the human DLBCL cell line with high MYC expression to the MYC inhibitor (MYCi, MYCi361); at doses reported (Selleckchem) to specifically inhibit MYC activity; for 72h, led to significant toxicity as measured by CellTitre-Glo assay (n=5). (B) Exposure of 11 human DLBCL cell lines with varying MYC protein expression; determined by Western blot with band intensities quantified using Image J normalized to VINCULIN; to physiologically attainable concentrations of MMF or AZD1775 indicated a correlation between MYC expression (low, blue; intermediate, orange; high, green) and increased AZD1775 cytotoxicity as measured by the CellTitre-Glo assay. (C) Dose response curves in two representative DLBCL cell lines show significant cytotoxicity with combined MMF and AZD1775 treatment in high MYC-expressing OCI-LY3 but not low MYC-expressing Farage. (D) Fold-change representing the ratio of the surviving fraction following exposure to various AZD1775+MMF dose combinations versus AZD1775 alone for the 11 human DLBCL cell lines. A fold change <0.8 indicates synergism and >1.2 indicates antagonism. Cell lines expressing high levels of MYC (green) are synergistically sensitive to the combined treatment. (E) Treatment of the OCI-LY3 cell line with a MYC inhibitor (MYCi,

MYCi361) reduced its sensitivity to single-agent MMF (1000nM) and combined treatment with MMF (1000nM) and AZD1775 (200nM) (n=5). Surviving fraction was normalized to the appropriate MYCi dose to highlight any rescue from MMF and/or AZD1775 toxicity. (F) Data-mining of the DepMap database reveals that protein expression of the top hits identified in the CRISPR/Cas9-mediated loss-of-function screen inversely correlate with MYC but not ATM expression in human DLBCL. (A,C,E) Cytotoxicity experiments were conducted on ≥5 separate occasions and data presented as mean ± SEM. Statistical significance versus Vehicle (*), MMF (†), AZD1775 (+), or MMF + MYCi (‡), was ascertained by matched multi-comparison (A) one-way or (C,E) two-way ANOVA with Tukey post-hoc test denoted by: *P≤0.05, **P≤0.01, ***P≤0.005, ****P≤0.001, *****P≤0.0005.

Figure 8. Nucleotide depletion induces replication stress-mediated apoptosis in human DLBCL cells with high MYC expression. (A-E) Exposure (72h) of OCI-LY3; a representative human DLBCL cell line with high MYC expression; to vehicle, MMF (1000nM) or AZD1775 (200nM), alone or in combination, led to (A,B) cell death primarily via apoptosis as ascertained by (A) DAPI staining (n=4) and confirmed by (B) AxV/PI status (n=4): viable (AxV^-/PI^-), early apoptotic (AxV^+/PI^-), late apoptotic (AxV^+/PI^+), and secondary necrotic (AxV^-/PI^+). (C) Cell cycle profiles showed an accumulation of cells in S-phase upon all treatments (n=4). (D) MMF (1000nM) treatment alone and in combination with AZD1775 (200nM) led to accumulation of non-replicating (inactive, EDU^-) cells residing in S-phase (n=4). (E) Replication stress response generated by either AZD1775 or MMF treatment is evident in the high MYC-expressing OCI-LY3 DLBCL cell line. Irradiated (IR, 6Gy, 30min) CII-ATM KD CLL cell line and A-T patient-derived LCLs serve as positive controls. Band intensities quantified using Image J were normalized to VINCULIN from ≥3 western blots. (F) Schematic summarizing the mechanistic basis of targeting nucleotide biosynthesis in MYC-overexpressing DLBCL. (A-E) Experiments were conducted on ≥3 separate occasions and data presented as mean ± SEM. Statistical significance versus Vehicle (red), MMF (orange), AZD1775 (blue), Viable (*), Early Apoptotic (†), Late Apoptotic or Inactive (+), or Necrotic (‡), was ascertained by matched multi-comparison (A) one-way or (B-D) two-way ANOVA with Tukey post-hoc test denoted by: *P≤0.05, **P≤0.01, ***P≤0.005, ****P≤0.001, *****P≤0.0005, ******P≤0.0001.

Figure 1

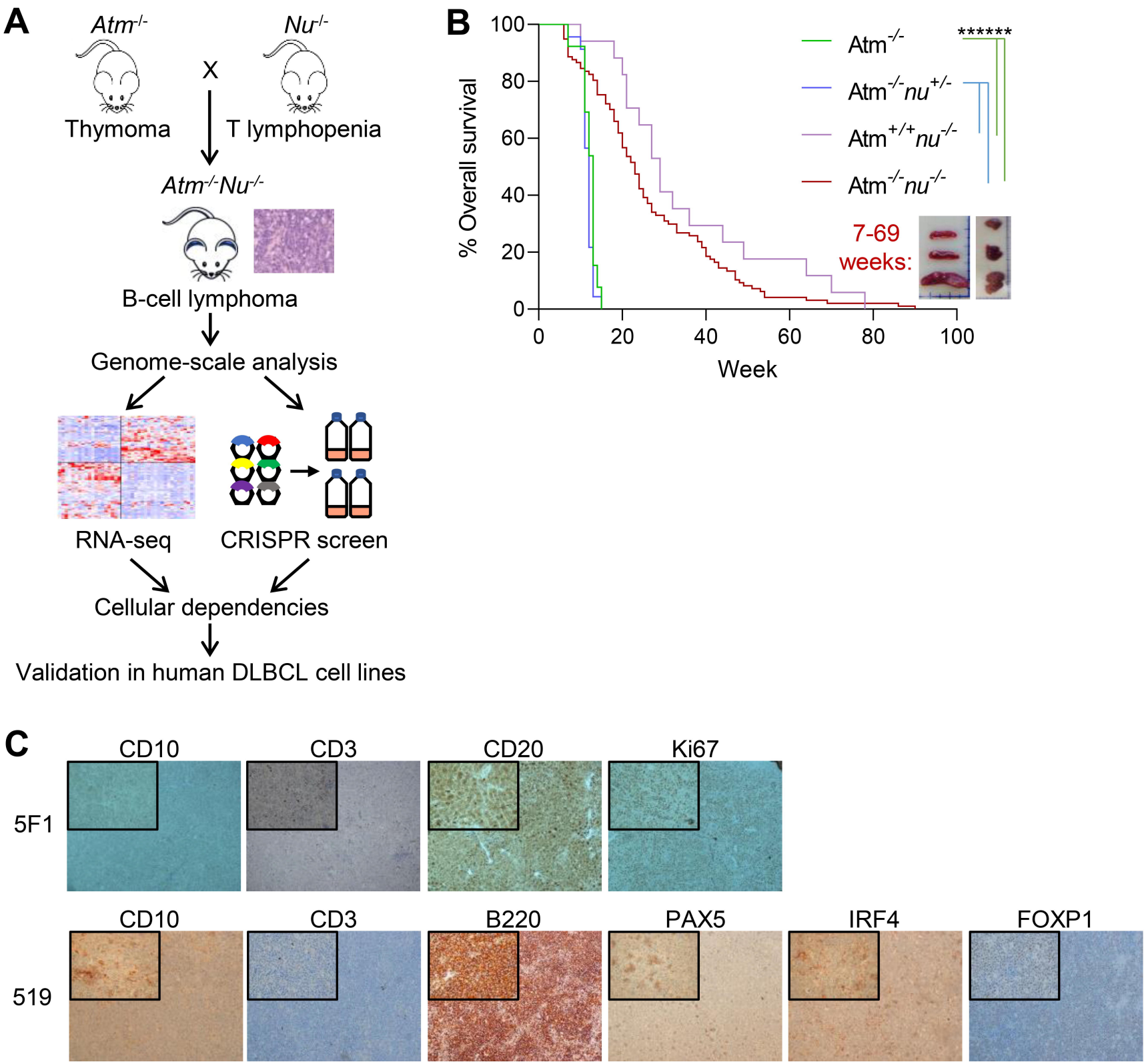
A
Atm-/-
Nu-/-
X
Thymoma
T lymphopenia
Atm-/-Nu-/-
B-cell lymphoma
Genome-scale analysis
RNA-seq
CRISPR screen
Cellular dependencies
Validation in human DLBCL cell lines
B
% Overall survival
Week
Atm-/-
Atm-/-nu+/-
Atm+/+nu-/-
Atm-/-nu-/-
******
7-69 weeks:
C
CD10
CD3
CD20
Ki67
5F1
CD10
CD3
B220
PAX5
IRF4
FOXP1
519

Figure 2

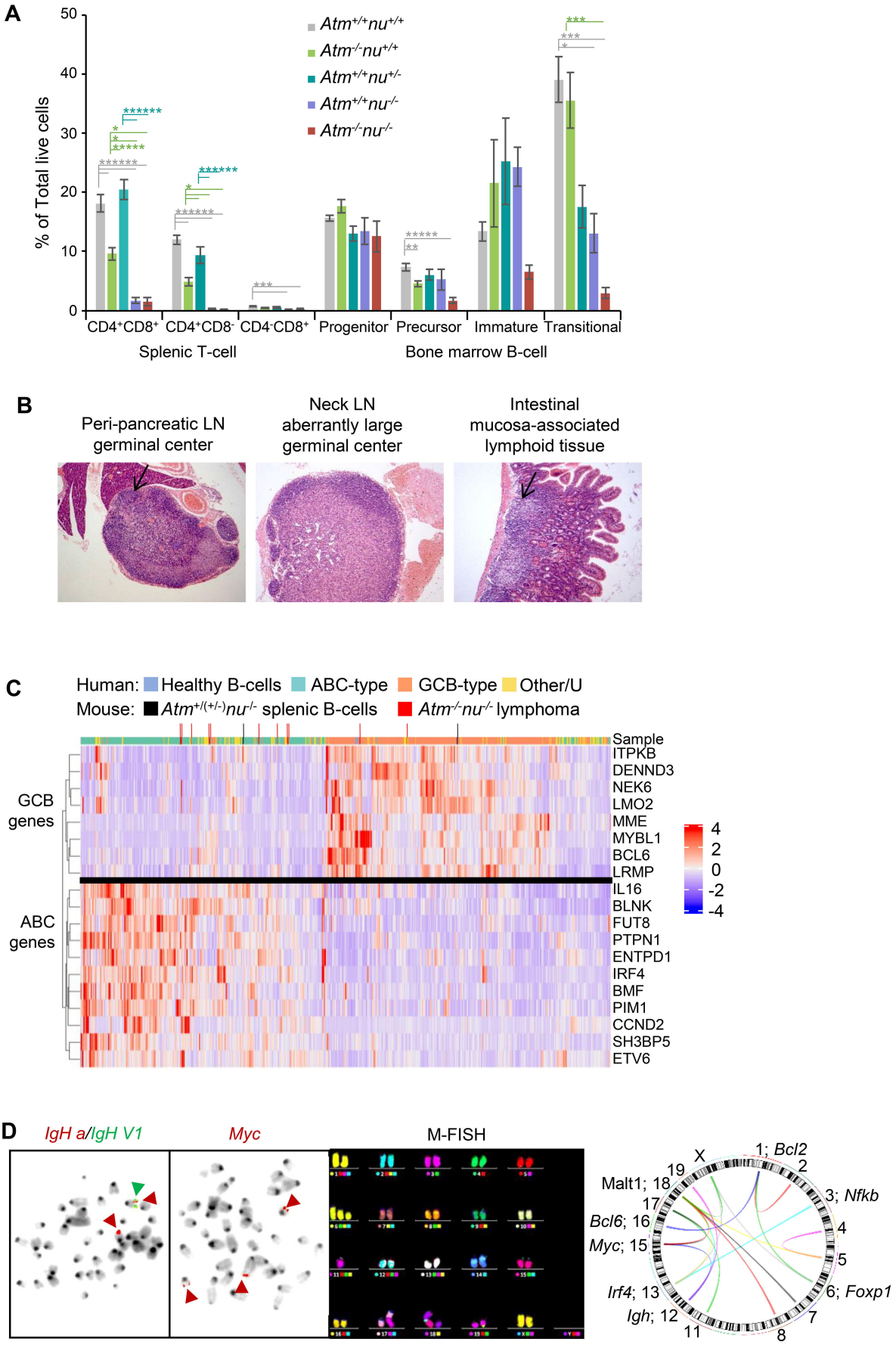
A
% of Total live cells
Atm+/+nu+/+
Atm-/-nu+/+
Atm+/+nu+/-
Atm+/+nu-/-
Atm-/-nu-/-
CD4+CD8+
CD4+CD8-
CD4-CD8+
Progenitor
Precursor
Immature
Transitional
Splenic T-cell
Bone marrow B-cell
B
Peri-pancreatic LN germinal center
Neck LN aberrantly large germinal center
Intestinal mucosa-associated lymphoid tissue
C
Human: Healthy B-cells ABC-type GCB-type Other/U
Mouse: Atm+/(+/-)nu-/- splenic B-cells Atm-/-nu-/- lymphoma
Sample
GCB genes
ABC genes
ITPKB
DENND3
NEK6
LMO2
MME
MYBL1
BCL6
LRMP
IL16
BLNK
FUT8
PTPN1
ENTPD1
IRF4
BMF
PIM1
CCND2
SH3BP5
ETV6
D
IgH a/IgH V1
Myc
M-FISH
Malt1; 18
Bcl6; 16
Myc; 15
Irf4; 13
Igh; 12
1; Bcl2
3; Nfkb
6; Foxp1

Figure 3

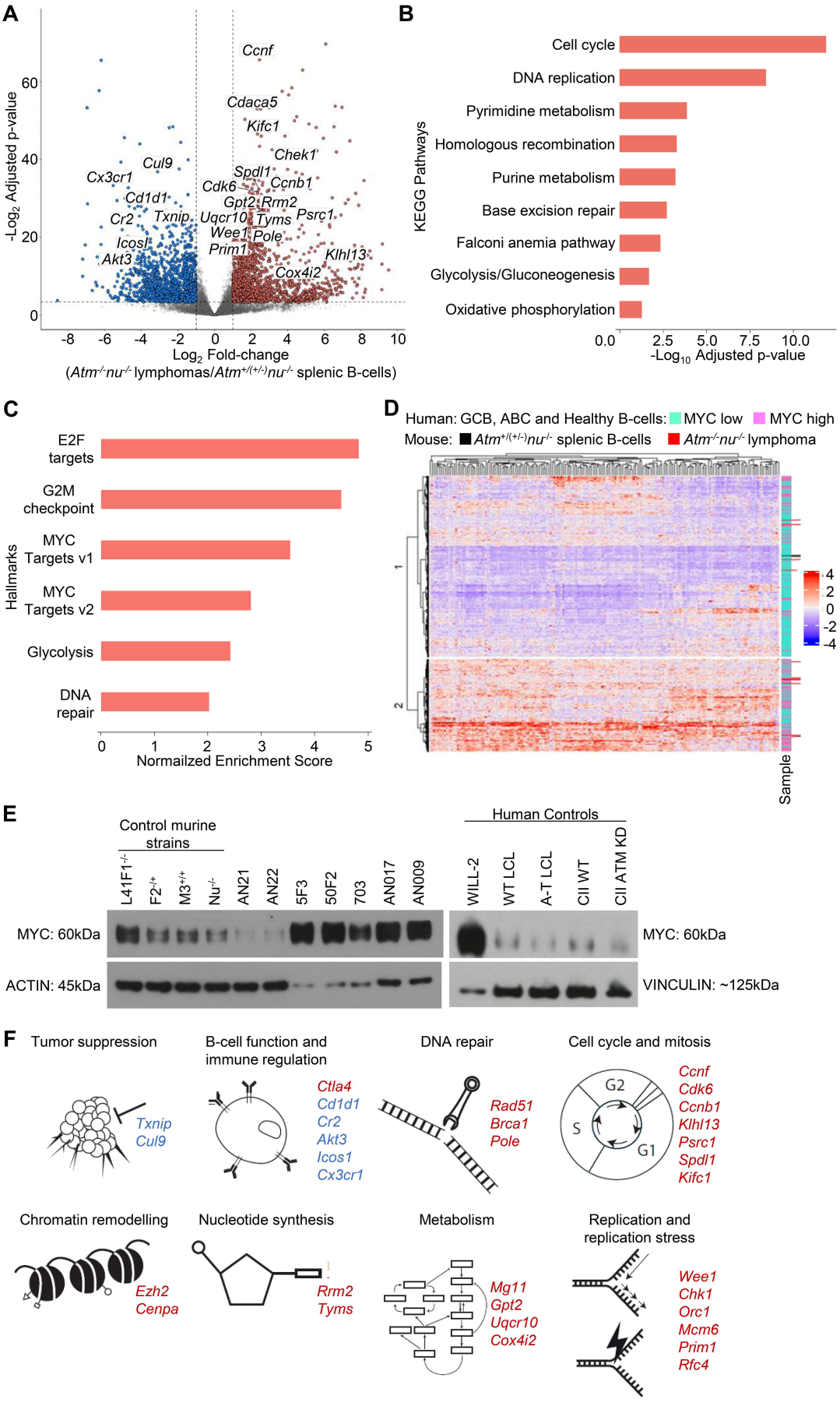
A
-Log2 Adjusted p-value
Log2 Fold-change
(Atm-/-nu-/- lymphomas/Atm+/(+/-)nu-/- splenic B-cells)
Ccnf
Cdaca5
Kifc1
Chek1
Spdl1
Ccnb1
Cdk6
Gpt2
Rrm2
Uqcr10
Tyms
Psrc1
Wee1
Pole
Prim1
Klhl13
Cox4i2
Cul9
Cx3cr1
Cd1d1
Cr2
Txnip
Icos
Akt3
B
KEGG Pathways
Cell cycle
DNA replication
Pyrimidine metabolism
Homologous recombination
Purine metabolism
Base excision repair
Falconi anemia pathway
Glycolysis/Gluconeogenesis
Oxidative phosphorylation
-Log10 Adjusted p-value
C
Hallmarks
E2F targets
G2M checkpoint
MYC Targets v1
MYC Targets v2
Glycolysis
DNA repair
Normailzed Enrichment Score
D
Human: GCB, ABC and Healthy B-cells: MYC low MYC high
Mouse: Atm+/(+/-)nu-/- splenic B-cells Atm-/-nu-/- lymphoma
Sample
E
Control murine strains
Human Controls
L41F1-/-
F2-/+
M3+/+
Nu-/-
AN21
AN22
5F3
50F2
703
AN017
AN009
WILL-2
WT LCL
A-T LCL
CII WT
CII ATM KD
MYC: 60kDa
ACTIN: 45kDa
VINCULIN: ~125kDa
F
Tumor suppression
Txnip
Cul9
B-cell function and immune regulation
Ctla4
Cd1d1
Cr2
Akt3
Icos1
Cx3cr1
DNA repair
Rad51
Brca1
Pole
Cell cycle and mitosis
G2
S
G1
Ccnf
Cdk6
Ccnb1
Klhl13
Psrc1
Spdl1
Kifc1
Chromatin remodelling
Ezh2
Cenpa
Nucleotide synthesis
Rrm2
Tyms
Metabolism
Mg11
Gpt2
Uqcr10
Cox4i2
Replication and replication stress
Wee1
Chk1
Orc1
Mcm6
Prim1
Rfc4

Figure 4

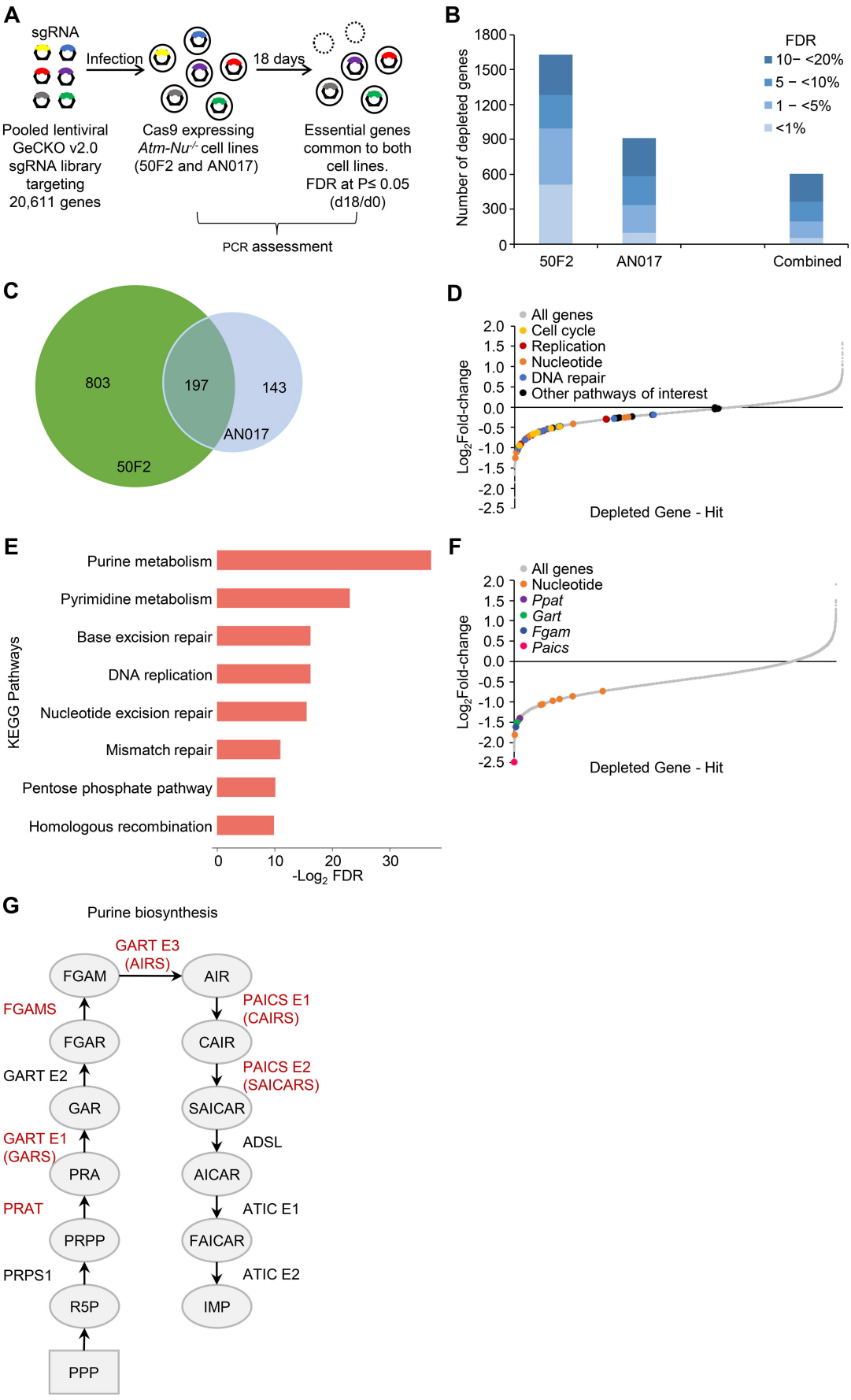
A
sgRNA
Infection
18 days
Pooled lentiviral GeCKO v2.0 sgRNA library targeting 20,611 genes
Cas9 expressing Atm-Nu-/- cell lines (50F2 and AN017)
Essential genes common to both cell lines. FDR at P≤ 0.05 (d18/d0)
PCR assessment
B
Number of depleted genes
1800
1500
1200
900
600
300
0
FDR
10– <20%
5 – <10%
1 – <5%
<1%
50F2
AN017
Combined
C
803
197
143
AN017
50F2
D
All genes
Cell cycle
Replication
Nucleotide
DNA repair
Other pathways of interest
Log2Fold-change
2.0
1.5
1.0
0.5
0.0
-0.5
-1.0
-1.5
-2.0
-2.5
Depleted Gene - Hit
E
KEGG Pathways
Purine metabolism
Pyrimidine metabolism
Base excision repair
DNA replication
Nucleotide excision repair
Mismatch repair
Pentose phosphate pathway
Homologous recombination
0
10
20
30
-Log2 FDR
F
All genes
Nucleotide
Ppat
Gart
Fgam
Paics
Log2Fold-change
Depleted Gene - Hit
G
Purine biosynthesis
GART E3 (AIRS)
FGAM
AIR
FGAMS
PAICS E1 (CAIRS)
FGAR
CAIR
GART E2
PAICS E2 (SAICARS)
GAR
SAICAR
GART E1 (GARS)
ADSL
PRA
AICAR
PRAT
ATIC E1
PRPP
FAICAR
PRPS1
ATIC E2
R5P
IMP
PPP

Figure 5

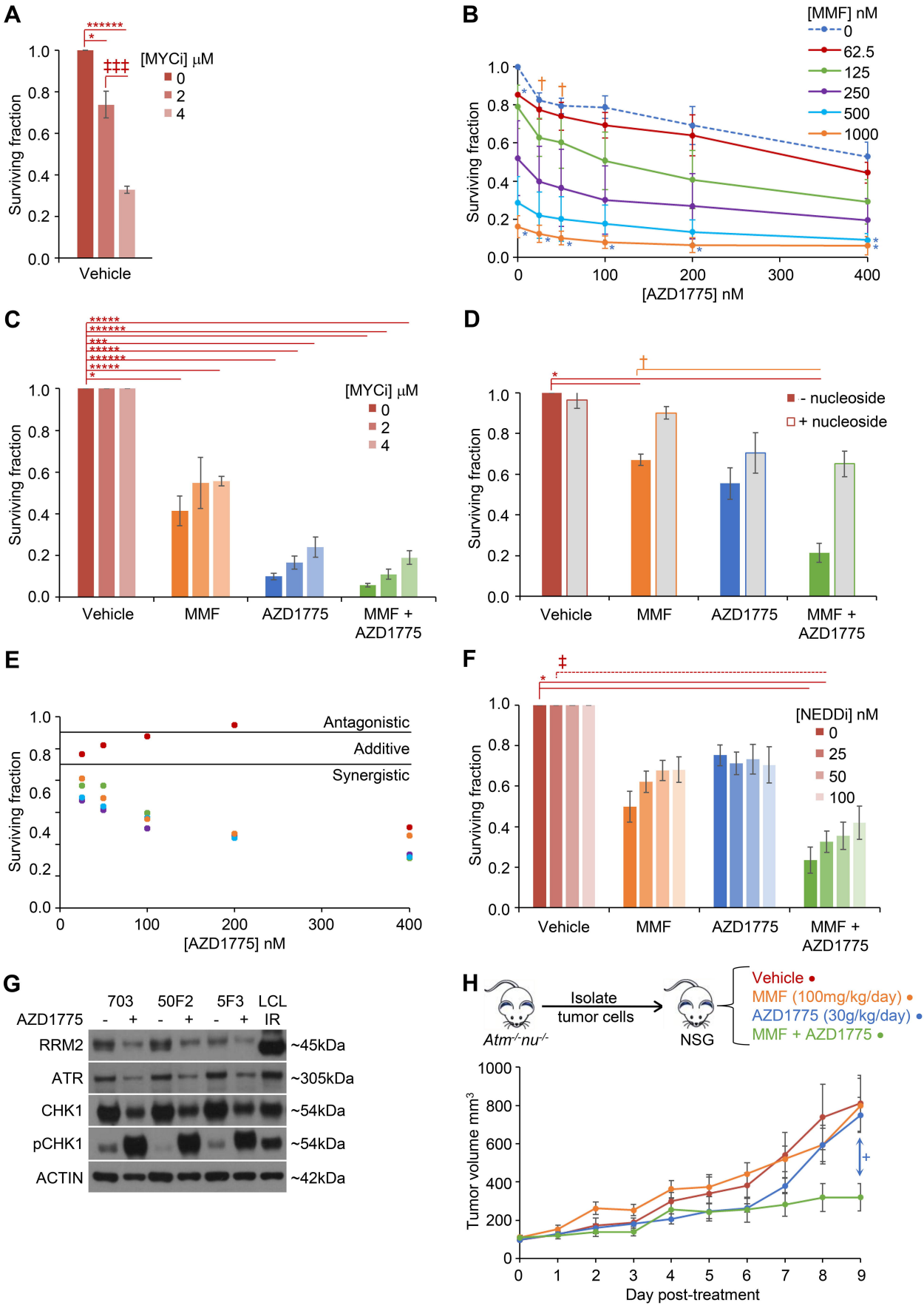
A
Surviving fraction
[MYCi] μM
0
2
4
Vehicle
B
[MMF] nM
0
62.5
125
250
500
1000
Surviving fraction
[AZD1775] nM
C
[MYCi] μM
0
2
4
Surviving fraction
Vehicle
MMF
AZD1775
MMF + AZD1775
D
- nucleoside
+ nucleoside
Surviving fraction
Vehicle
MMF
AZD1775
MMF + AZD1775
E
Antagonistic
Additive
Synergistic
Surviving fraction
[AZD1775] nM
F
[NEDDi] nM
0
25
50
100
Surviving fraction
Vehicle
MMF
AZD1775
MMF + AZD1775
G
703
50F2
5F3
LCL
AZD1775
- + - + - + IR
RRM2
ATR
CHK1
pCHK1
ACTIN
~45kDa
~305kDa
~54kDa
~54kDa
~42kDa
H
Isolate tumor cells
Atm-/-nu-/-
NSG
Vehicle
MMF (100mg/kg/day)
AZD1775 (30g/kg/day)
MMF + AZD1775
Tumor volume mm3
Day post-treatment

Figure 6

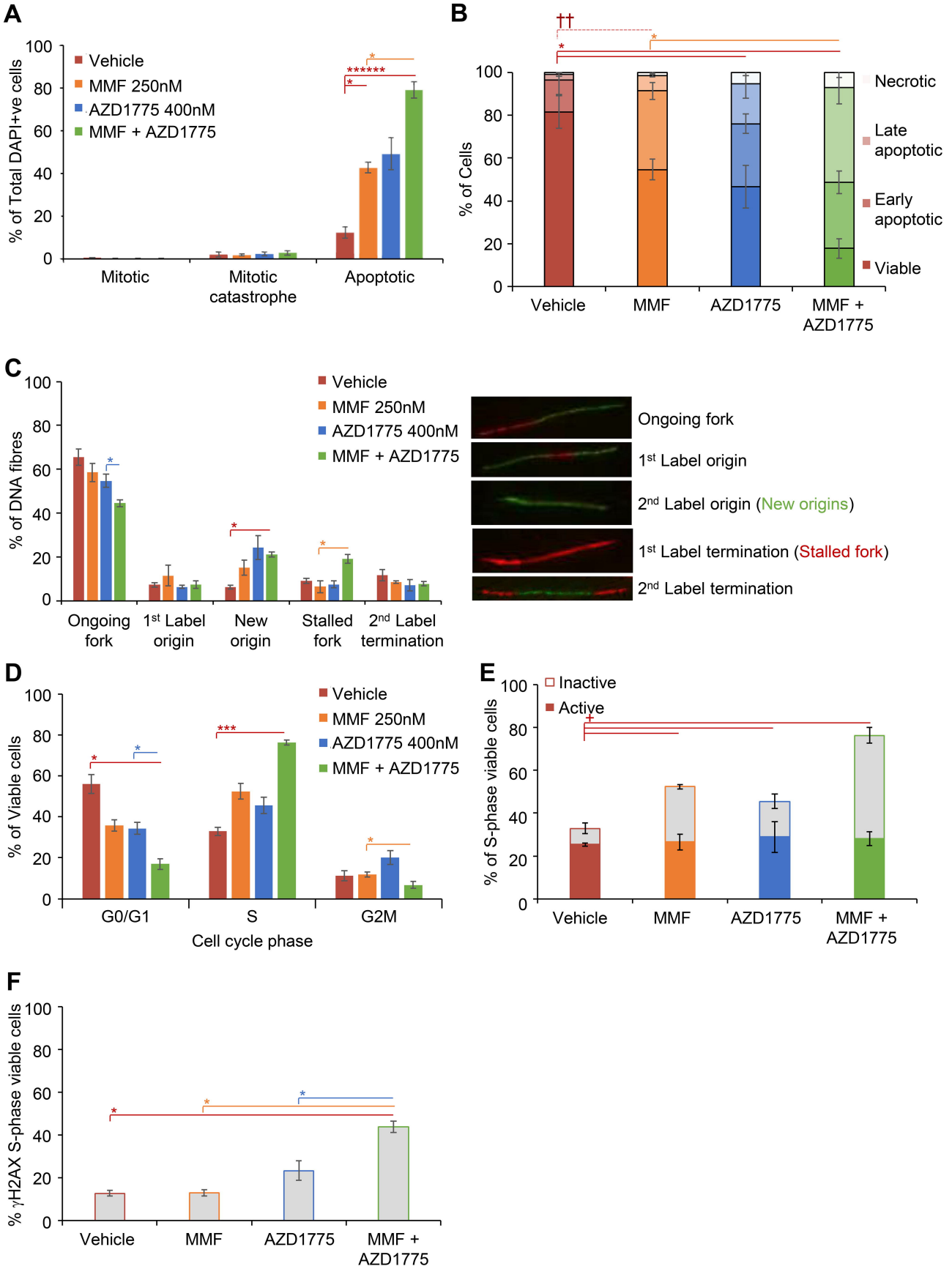
A
% of Total DAPI+ve cells
Vehicle
MMF 250nM
AZD1775 400nM
MMF + AZD1775
Mitotic
Mitotic catastrophe
Apoptotic
B
% of Cells
Necrotic
Late apoptotic
Early apoptotic
Viable
Vehicle
MMF
AZD1775
MMF + AZD1775
C
% of DNA fibres
Ongoing fork
1st Label origin
New origin
Stalled fork
2nd Label termination
2nd Label origin (New origins)
1st Label termination (Stalled fork)
D
% of Viable cells
G0/G1
S
G2M
Cell cycle phase
E
Inactive
Active
% of S-phase viable cells
F
% γH2AX S-phase viable cells

Figure 7

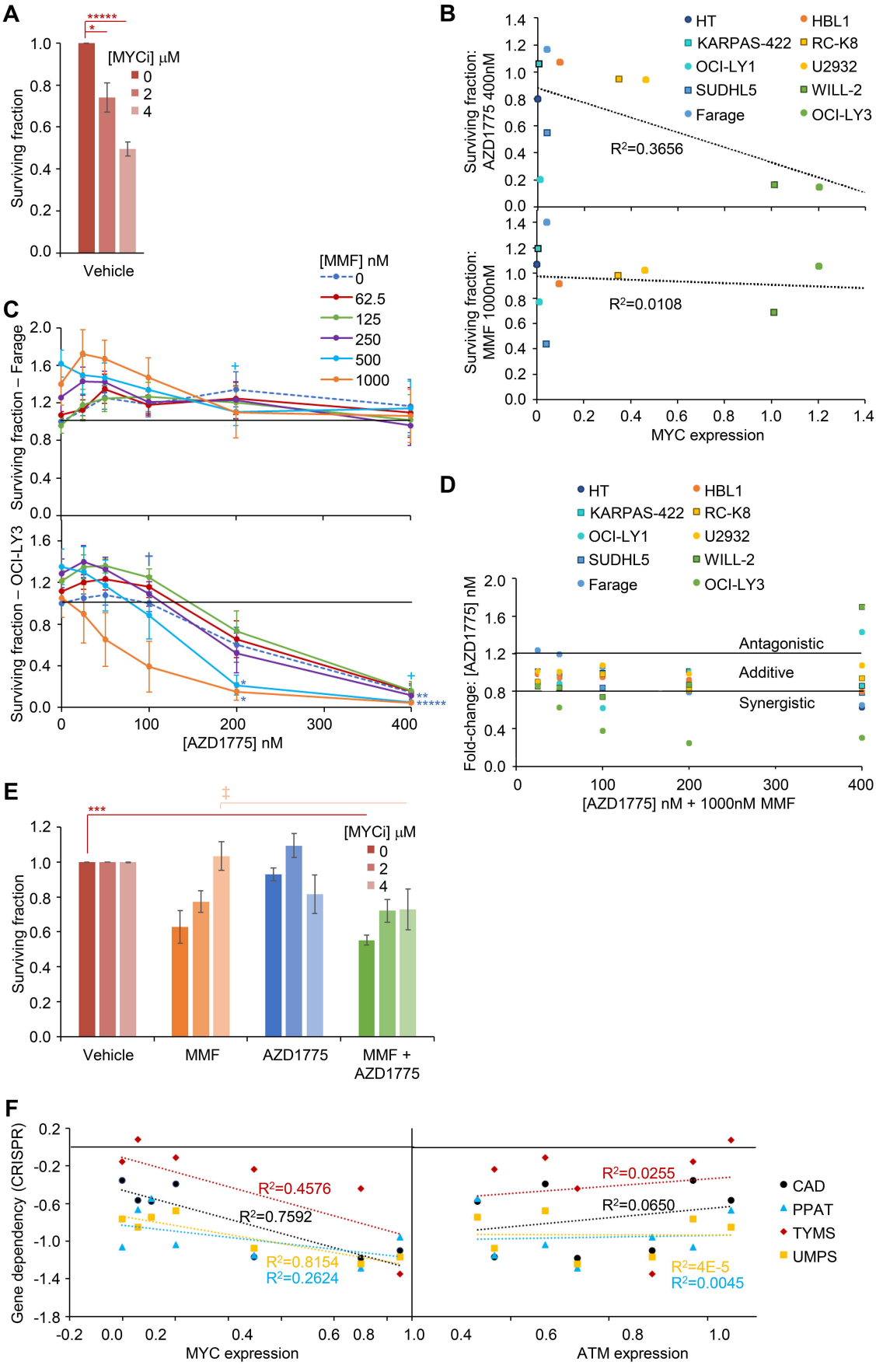
A
Surviving fraction
[MYCi] μM
0
2
4
Vehicle
B
Surviving fraction: AZD1775 400nM
Surviving fraction: MMF 1000nM
HT
HBL1
KARPAS-422
RC-K8
OCI-LY1
U2932
SUDHL5
WILL-2
Farage
OCI-LY3
R²=0.3656
R²=0.0108
MYC expression
C
Surviving fraction – Farage
Surviving fraction – OCI-LY3
[MMF] nM
0
62.5
125
250
500
1000
[AZD1775] nM
D
Fold-change: [AZD1775] nM
Antagonistic
Additive
Synergistic
[AZD1775] nM + 1000nM MMF
E
Surviving fraction
[MYCi] μM
Vehicle
MMF
AZD1775
MMF + AZD1775
F
Gene dependency (CRISPR)
R²=0.4576
R²=0.7592
R²=0.8154
R²=0.2624
R²=0.0255
R²=0.0650
R²=4E-5
R²=0.0045
MYC expression
ATM expression
CAD
PPAT
TYMS
UMPS

Figure 8

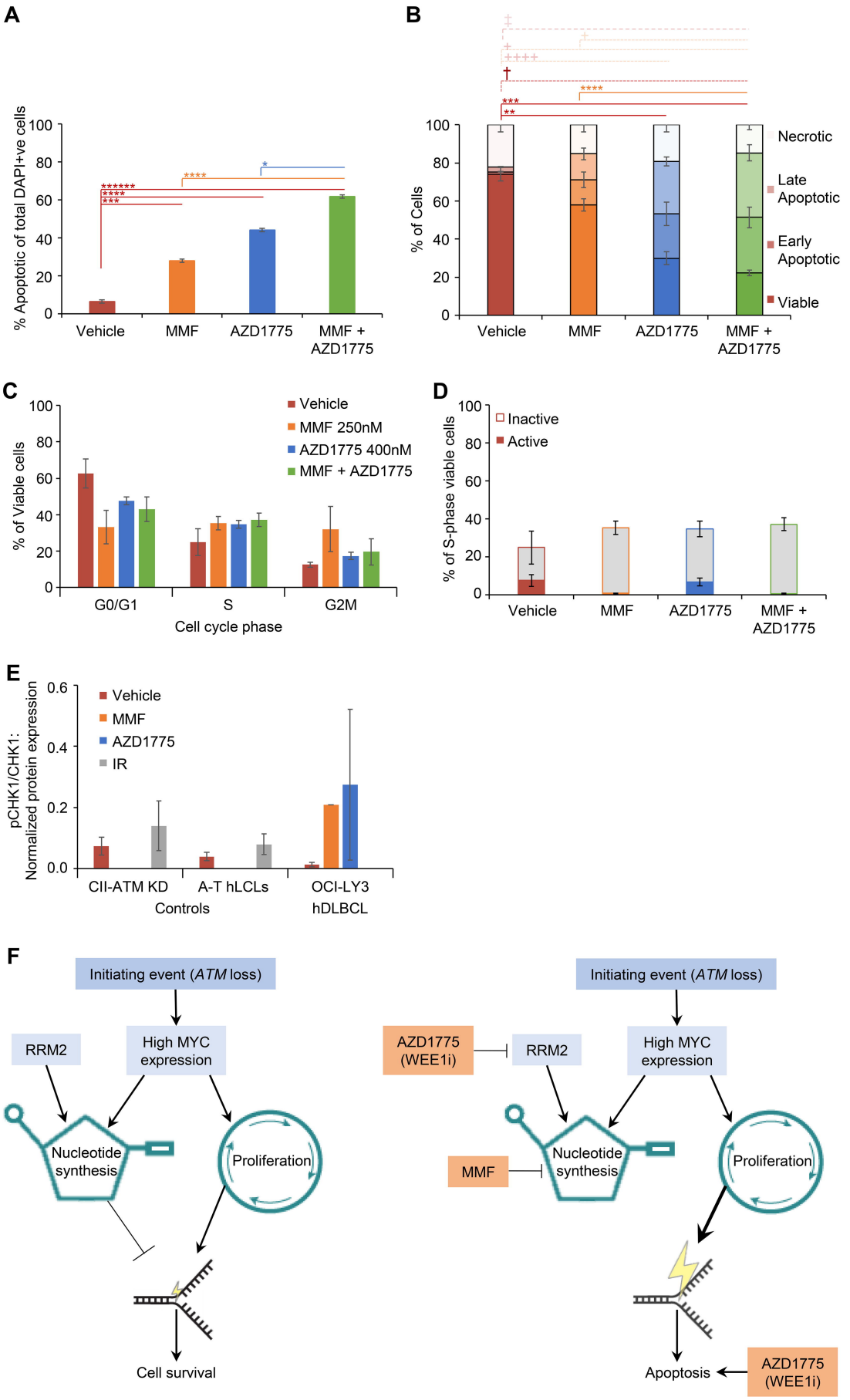
A
% Apoptotic of total DAPI+ve cells
Vehicle
MMF
AZD1775
MMF + AZD1775
B
% of Cells
Necrotic
Late Apoptotic
Early Apoptotic
Viable
C
% of Viable cells
Vehicle
MMF 250nM
AZD1775 400nM
MMF + AZD1775
G0/G1
S
G2M
Cell cycle phase
D
% of S-phase viable cells
Inactive
Active
E
pCHK1/CHK1: Normalized protein expression
Vehicle
MMF
AZD1775
IR
CII-ATM KD
A-T hLCLs
OCI-LY3 hDLBCL
Controls
F
Initiating event (ATM loss)
RRM2
High MYC expression
Nucleotide synthesis
Proliferation
Cell survival
AZD1775 (WEE1i)
MMF
Apoptosis

Supplementary Material

Supplementary Methods

Genotyping of *Atm*$^{-/-}$*nu*$^{-/-}$ mice

Atm genotype was confirmed by PCR, utilizing primer pairs that recognize a consensus *Atm* sequence.[1]

Cell lines

Human DLBCL cell lines were obtained from DSMZ (Braunschweig, Germany; BJAB, HT, OCI-LY1, OCI-LY3, RC-K8, SUDHL5, U2932, WILL-2), ATCC (Manassas, VA; Farage, HBL1) or ECACC (Porton Down, UK; KARPAS-422). Human Burkitt lymphoma cell lines were obtained from DSMZ (BJAB, DG75). Lymphoblastoid cell lines (LCL) were previously generated.[2] The CII-*ATM/GFP* CLL cell lines were previously generated from CII (obtained from Prof. A Rosen, Linkoping University, Sweden).[2] All human cell lines were cultured in RPMI containing 10% FCS and 1% penicillin/streptomycin.

Murine *Eμ–Myc* cell lines; modelling Burkitt lymphoma; were established from Eμ-Myc transgenic lymphomas.[3]

Cytotoxicity assays

Cell lines were treated with MMF, AZD1775, pevonedistat (MLN4924; Selleckchem), MYC inhibitor (MYCi361; Selleckchem) and nucleosides (Sigma-Aldrich, Poole, UK) either alone or in combination. Cytotoxicity was determined by alamar blue uptake (Sigma-Aldrich), CellTiter-Glo (Promega, Southampton, UK), or propidium iodide (PI; Sigma-Aldrich) exclusion, and analyzed using a PHERAstar (BMG Labtech, Aylesbury, UK) or Enspire (PerkinElmer, Beaconsfield, UK) microplate reader or LSRFortessa™ X-20 Cell Analyzer (BD Biosciences, Oxford, UK). All experiments were performed at least in triplicate. Combination indices (CI) to identify synergism and 50% effective concentration (EC_{50}) were calculated using CalcuSyn (Biosoft, Cambridge, UK).

V(D)J recombination analysis

Sanger sequencing of *V(D)J* rearrangements was undertaken according to standard protocols.[4] Analysis was carried out using the NCBI Ig Blast software.

FACS analysis

Cells were analyzed using a CyAn ADP FACS analyzer (Beckman Coulter, High Wycombe, UK) and Summit software (v4.3). Non-specific antibody binding was blocked by anti-mouse CD16/32 before staining with CD3, CD4-PE, CD8a-APC, CD5-APC, B220-E450, CD43-PE, IgM and IgD antibodies (eBiosciences, Altrincham, UK).

Cell cycle analysis was performed according to standard methods.[5] Apoptosis was determined with an Annexin V (AxV) Apoptosis Detection kit (eBiosciences). γH2AX expression was determined using γH2AX-FITC antibody (Millipore, Watford, UK) and the Click-iT™ EdU Alexa Fluor™ 647 Flow Cytometry Assay Kit (ThermoFisher, Gloucester, UK). All analysed using the BD LSRFortessa™ X-20 and FlowJo v10.8.0.

Immunohistochemistry

Immunohistochemistry was performed using antibodies against B220 (BD Biosciences), CD20 (Life Technologies), CD21 (Abcam, Cambridge, UK), CD10 (Bioss, Boston, MA), CD3, IRF4 (Dako, Cambridge, UK; Abcam), BCL2 (Novus, Abingdon, UK), Ki67, PAX5 (BD Biosciences), and FOXP1 (AbD Serotec, Watford, UK).[6]

RNA-seq analysis

RNA was isolated from *Atm*$^{-/-}$*nu*$^{-/-}$ lymphomas and *Atm*$^{+/+}$*nu*$^{-/-}$ or *Atm*$^{+/-}$*nu*$^{-/-}$ splenic B-cells using the RNeasy Micro Kit (Qiagen, Manchester, UK), quantified using Qubit, and quality assessed using TapeStation (Agilent, Manchester, UK). RNA-seq libraries generated using Neoprep mRNA kits (Illumina, Cambridge, UK) were sequenced on the NextSeq 500 platform (Illumina). For comparison, RNA-seq data of human DLBCL from the Cancer Genome Characterization Initiative (CGCI) study was downloaded from dbGap (http://www.ncbi.nlm.nih.gov/gap; accession phs000532)[7] and the European Genome-Phenome Archive (EGAS00001002606).[15] RNA-seq data for the control germinal center (GC) B-cell samples were obtained from the Gene Expression Omnibus (GEO; http://www.ncbi.nlm.nih.gov/geo/; accession GSE45982).[8]

Murine and human transcriptome data were aligned to GRCm38.p5 and hg19 respectively using Rsubread aligner, and assigned to individual genes using the Counts function (data available upon request).[9] The edgeR package in R was used to normalize read counts between samples, convert to counts-per-million (CPM) reads for each gene and analyze differential expression between sample groups.[10] Genes were considered to be differentially expressed if fold-change >2 and Benjamini-Hochberg adjusted P<0.05. Differential expression heatmaps were constructed using the gplots and ComplexHeatmap library in R. CPM values for each relevant gene were centered at zero, scaled separately and capped at +/- 3 before applying the Euclidean distance measure in conjunction with the Ward.D2 clustering algorithm. Kyoto Encyclopaedia of Genes and Genomes (KEGG) pathway analysis and Gene Set Enrichment Analysis (GSEA v3.0) were executed using clusterProfiler package in R.[11,12]

Fluorescence in situ hybridization (FISH)

Metaphases (≤40) were analyzed using the ISIS software (Didcot, UK) and images captured using a Zeiss Axio imager (Birmingham, UK).[13,14] The murine chromoprobe multiprobe octochrome system was used for M-FISH (Cytocell, Bicester, UK). Targeted-FISH probes were custom made from the following BAC: IgH alpha-5-ROX dUTP (RP23-455J10), IgH V1 5-Fluorescein dUTP (RP23-303N6) and c-Myc 5-ROX dUTP (RP23-307D14) (Empire Genomics, Buffalo, NY). Circos plots of chromosomal translocations were created using the Rcircos library in R.[15]

Western Blotting

Western blotting was performed using ATM (Sigma-Aldrich; Abcam), phospho (p)-ATM (Millipore), NBS1, p-NBS1 (Abcam), SMC1 (Bethyl, Montgomery, Texas, USA), MYC, RRM2, ATR, CHK1 (Santa Cruz, Wembley, UK), p-CHK1 (Cell Signaling, Leiden, Netherlands) VINCULIN or ACTIN (Sigma-Aldrich) primary antibodies and HRP-conjugated anti-rabbit or anti-mouse secondary antibodies (Dako). Immunoreactive bands were visualized using ECL solution and X-Ray film (GE Healthcare Life Sciences, Amersham, UK).[4]

Immunocytochemistry

Cell death was evaluated using 4',6-diamidino-2-phenylindole (DAPI; Sigma-Aldrich) counterstaining, goat anti–Lamin B (Atlas Antibodies, Stockholm, Sweden) and rabbit anti-p-

Histone H3 serine-10 (Cell Signaling) primary antibodies and anti-mouse (Alexa Fluor™ 594) and anti–rabbit (Alexa Fluor™ 488; Life Technologies) secondary antibodies[2] At least 100 cells were analyzed using a Nikon Eclipse E600 (Surbiton, Surrey).

DNA Fiber analysis

DNA fiber analysis was performed according to established protocols using idodeoxyuridine (IdU; Sigma-Aldrich), chlorodeoxyuridine (cldU; Sigma-Aldrich), rat- and mouse-bromodeoxyuridine (BrdU) antibodies (Abcam; BD Biosciences).[16] DNA fibers were analyzed using ImageJ.

Supplementary Figures

Figure S1. *Atm*$^{-/-}$*nu*$^{-/-}$ mice that develop lymphoma have prolonged overall survival irrespective of the cause of death

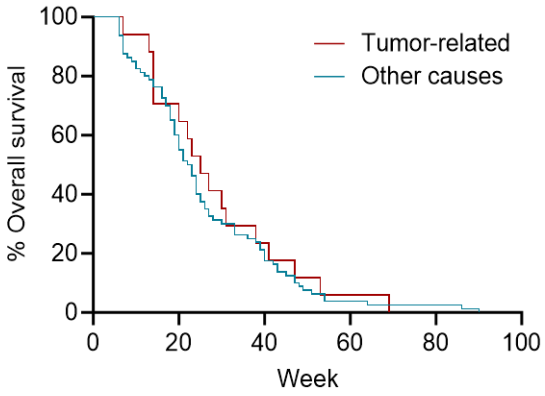

Kaplan-Meier curves displaying equivalent overall survival of *Atm*$^{-/-}$*nu*$^{-/-}$ mice that have died due to lymphoma or other causes including infection ($P \leq 0.05$).

Figure S2. *Atm*$^{-/-}$*nu*$^{-/-}$ mice develop B-cell lymphomas with complex karyotype that closely model human activated B-cell-like (ABC) and germinal center B-cell-like (GCB) diffuse large B-cell lymphoma (DLBCL)

A

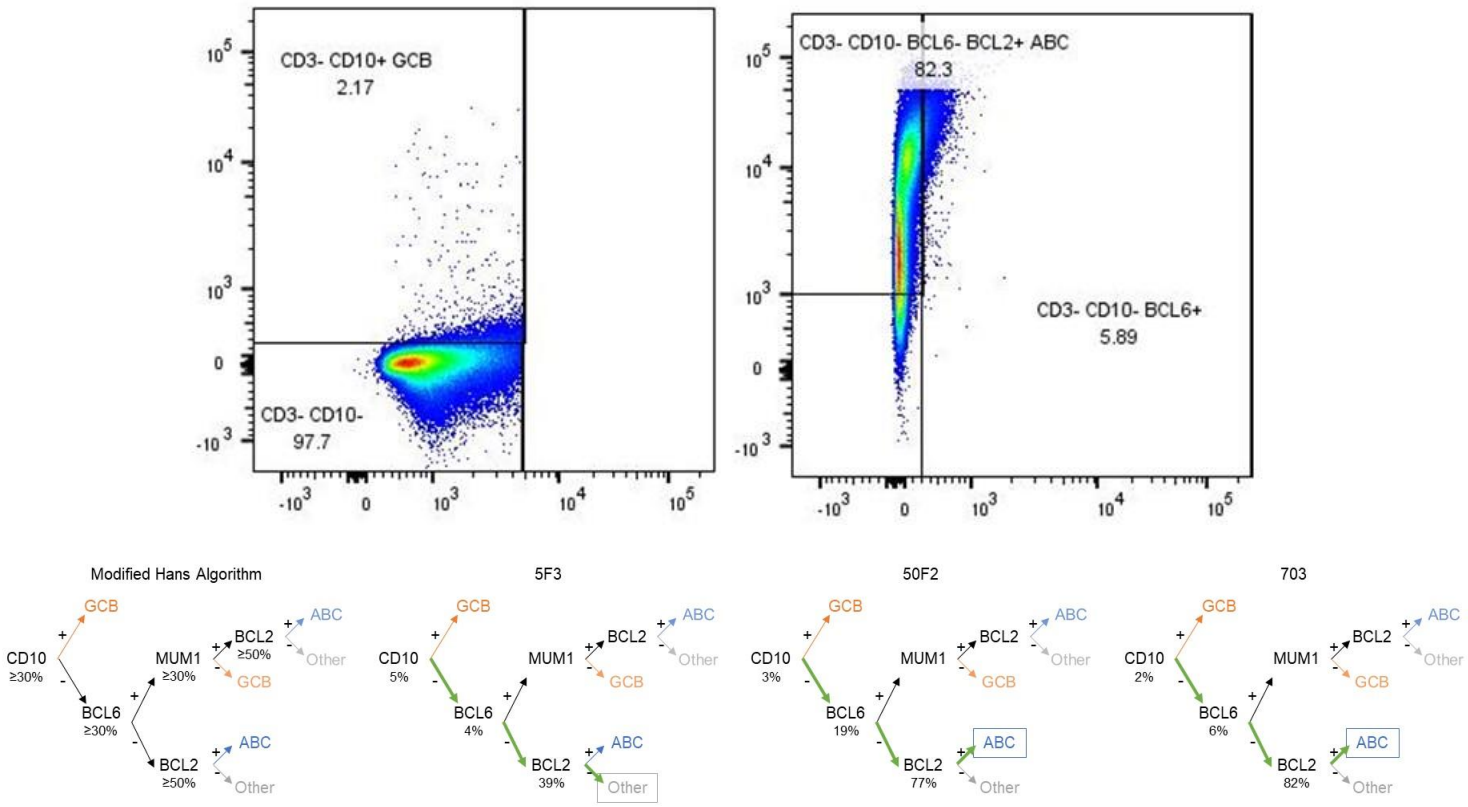

B

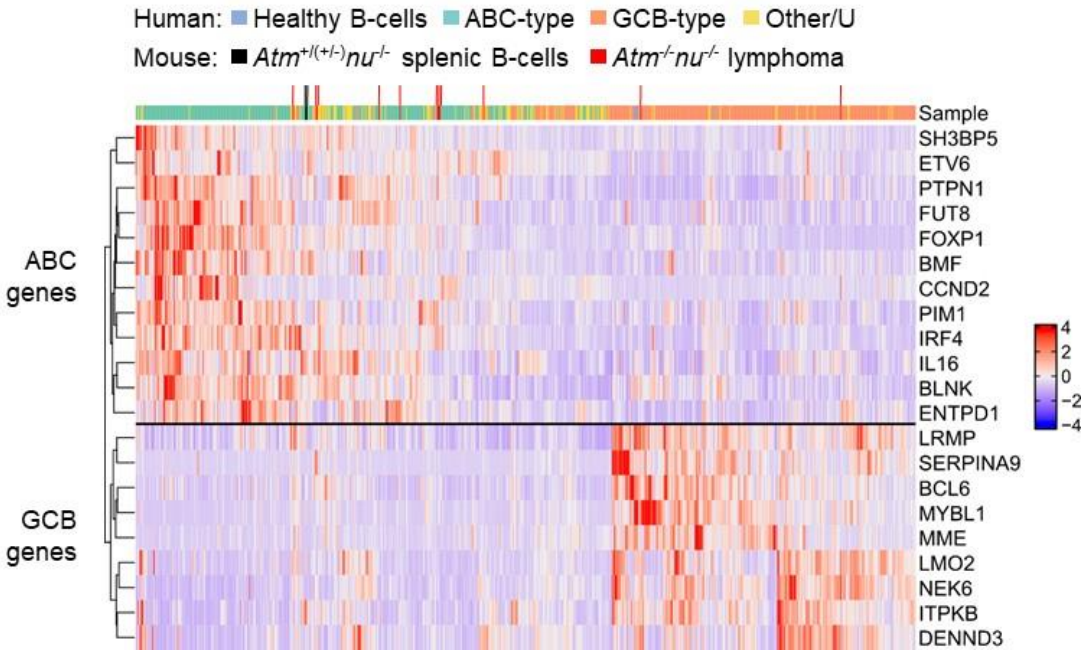

C

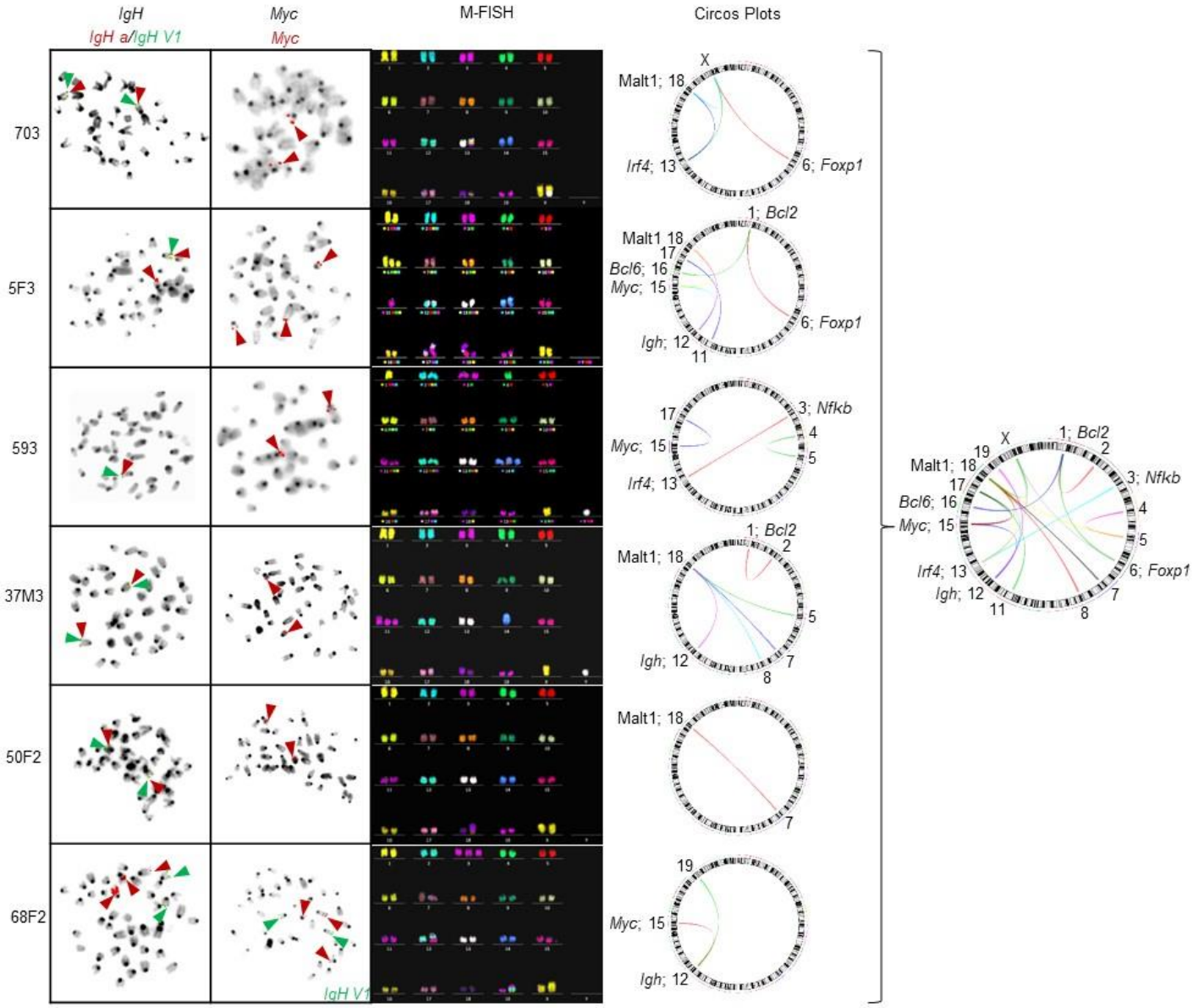

Characterization of the tumors derived from the *Atm*$^{-/-}$*nu*$^{-/-}$ murine model. (A) Identification of cellular phenotype by FACS analysis of three cell lines established from *Atm*$^{-/-}$*nu*$^{-/-}$ lymphomas (5F3, 50F2 and 703). Top: Representative FACS plots (703). Bottom: Cells compromising the murine DLBCL cell lines were classified as ABC (blue), GCB (orange) or other (grey) by sequential gating of subpopulations according to the Hans algorithm (https://www.leukaemia.org.nz/content/uploads/2019/11/DLBCL-LNZ-Protocol-2019.pdf) modified with the addition of BCL2 to differentiate non-GCB into ABC (BCL2^{+}) and other (BCL2^{-}) subtypes. The minimum percentage of cells expressing the marker to be considered positive for by immunohistochemistry is shown in the left hand diagram. Corresponding FACS analysis indicates that 50F2 and 703 cell lines are ABC DLBCL and 5F3 is other DLBCL. The outcome was confirmed upon replacement of MUM1 with FOXP1. (B) Comparison of

ribonucleic acid (RNA)-seq data of *Atm*$^{-/-}$*nu*$^{-/-}$ lymphomas (n=11) and control splenic B-cells from *Atm*$^{+/+}$*nu*$^{-/-}$ and *Atm*$^{+/-}$*nu*$^{-/-}$ mice (n=2) against published RNA-seq datasets of human ABC DLBCL and healthy control germinal center (GC) B-cells[7,8] suggests that the majority of *Atm*$^{-/-}$*nu*$^{-/-}$ lymphomas cluster with human ABC DLBCL.[17] (C) Specific translocations involving *IgH* and *MYC*, that are known drivers of MYC overexpression in human DLBCL, were specifically probed for by targeted-FISH whilst multiple cytogenetic alterations were detected by M-FISH in six representative *Atm*$^{-/-}$*nu*$^{-/-}$ DLBCL. A normal metaphase spread should depict two copies of each targeted gene, with co-localization of the two *IgH* probes, as indicated by the arrows (703, 37M3, 50F2; *IgHa*, red; *IgHVi*, green; *Myc*, red). Differing copy numbers indicate gains and losses of the relevant gene (5F3, 593, 68F2). Translocations of the *IgH* locus were evidenced by non-co-localized staining of the *IgHa* and *IgHVi* probes, upon evidence of which, spreads were assessed for co-localization of *Myc* and *IgHVi* probes to identify whether *IgH-Myc* fusion had occurred (68F2). Whilst there was no evidence that *Atm*$^{-/-}$*nu*$^{-/-}$ DLBCL harbored the human DLBCL *IgH-MYC* fusion, other abnormalities were detected: *Myc* gain (5F3, 68F2), *IgH* loss (5F3, 593), *IgH* translocation (68F2). The Circos plots depict the chromosomal interactions derived from identified aberrations for individual tumors and all 6 representative *Atm*$^{-/-}$*nu*$^{-/-}$ B-cell lymphoma combined. Chromosomes are indicated by the numerals and annotated with lymphoma relevant genes localized in the regions affected by chromosomal alterations. No common translocation was observed.

Figure S3. *Myc* and *Myc* target gene expression is upregulated in *Atm*$^{-/-}$*nu*$^{-/-}$ lymphomas

A

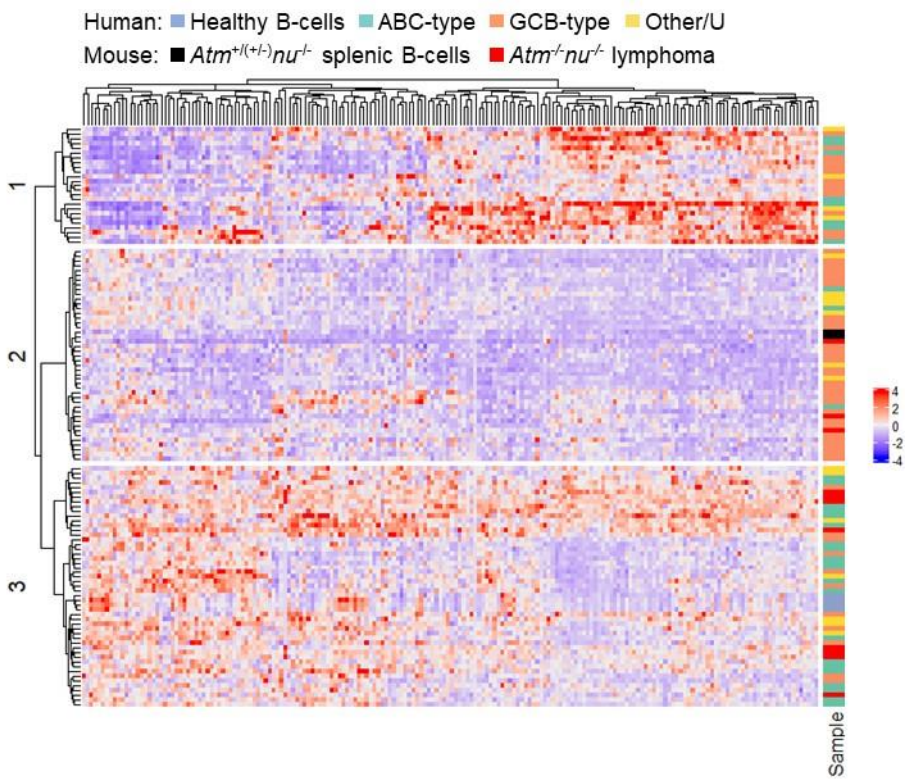

B

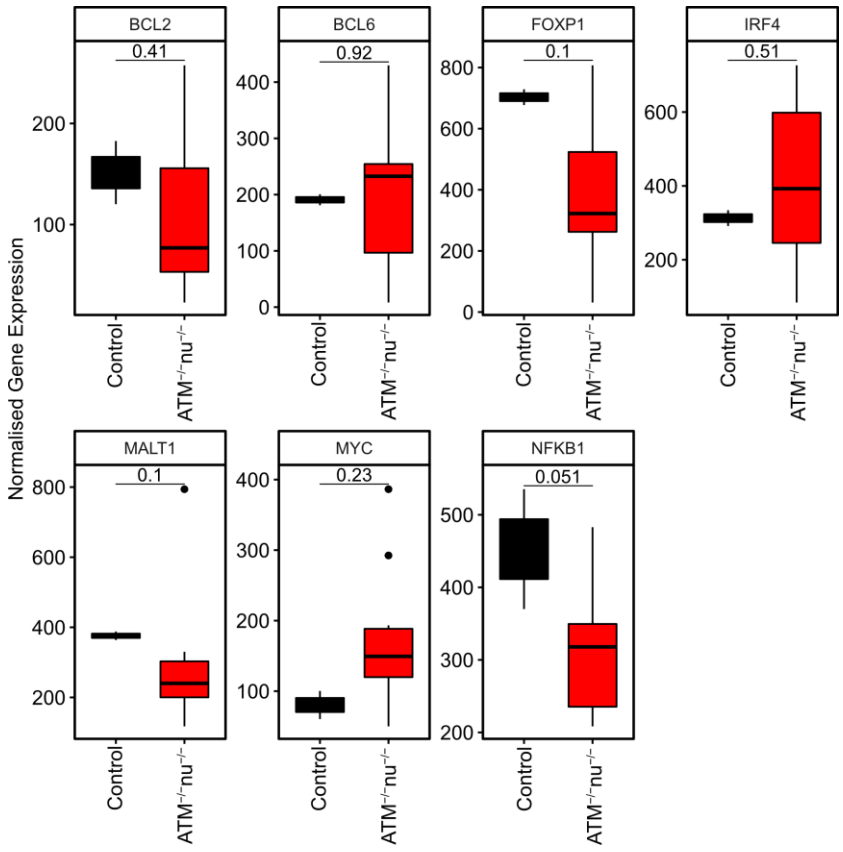

C

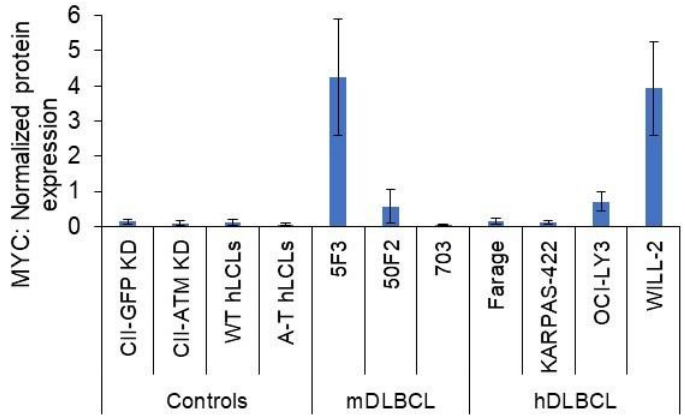

(A) Alignment of the transcriptional profiles of *Atm*$^{-/-}$*nu*$^{-/-}$ lymphomas (n=12) and control splenic B-cells from *Atm*$^{+/+}$*nu*$^{-/-}$ and *Atm*$^{+/-}$*nu*$^{-/-}$ mice (n=2), human ABC DLBCL[7] (n=32), GCB DLBCL[7] (n=54), other/unknown (U) DLBCL (n=18) and healthy control GC B-cells[8] (n=4) according to the expression of MYC target genes.[18] This reveals that a high proportion of *Atm*$^{-/-}$*nu*$^{-/-}$ DLBCL (red) align with a high (subset 3) MYC target gene-expressing group, whereas the *Atm*$^{+/+}$*nu*$^{-/-}$ and *Atm*$^{+/-}$*nu*$^{-/-}$ controls (black) align with the low (subset 2) MYC target gene-expressing group. (B) Compared to controls, RNA-seq analysis of *Atm*$^{-/-}$*nu*$^{-/-}$ lymphomas (n=11) suggests differential upregulation of MYC but not other lymphoma relevant genes. (C) In comparison to human ATM WT and deficient tumor (CLL CII-cell line) and non-tumor (three healthy and A-T patient-derived LCL) controls, MYC protein expression is upregulated in two cell lines established from *Atm*$^{-/-}$*nu*$^{-/-}$ lymphomas (5F3 and 50F2) and some human DLBCL cell lines (OCI-LY3 and WILL-2). Band intensities quantified using Image J were normalized to VINCULIN from ≥3 western blots and presented as mean ± SEM.

Figure S4. Cellular dependency pathways of *Atm*$^{-/-}$*nu*$^{-/-}$ lymphomas identified by a genome-wide CRISPR/Cas9 screen

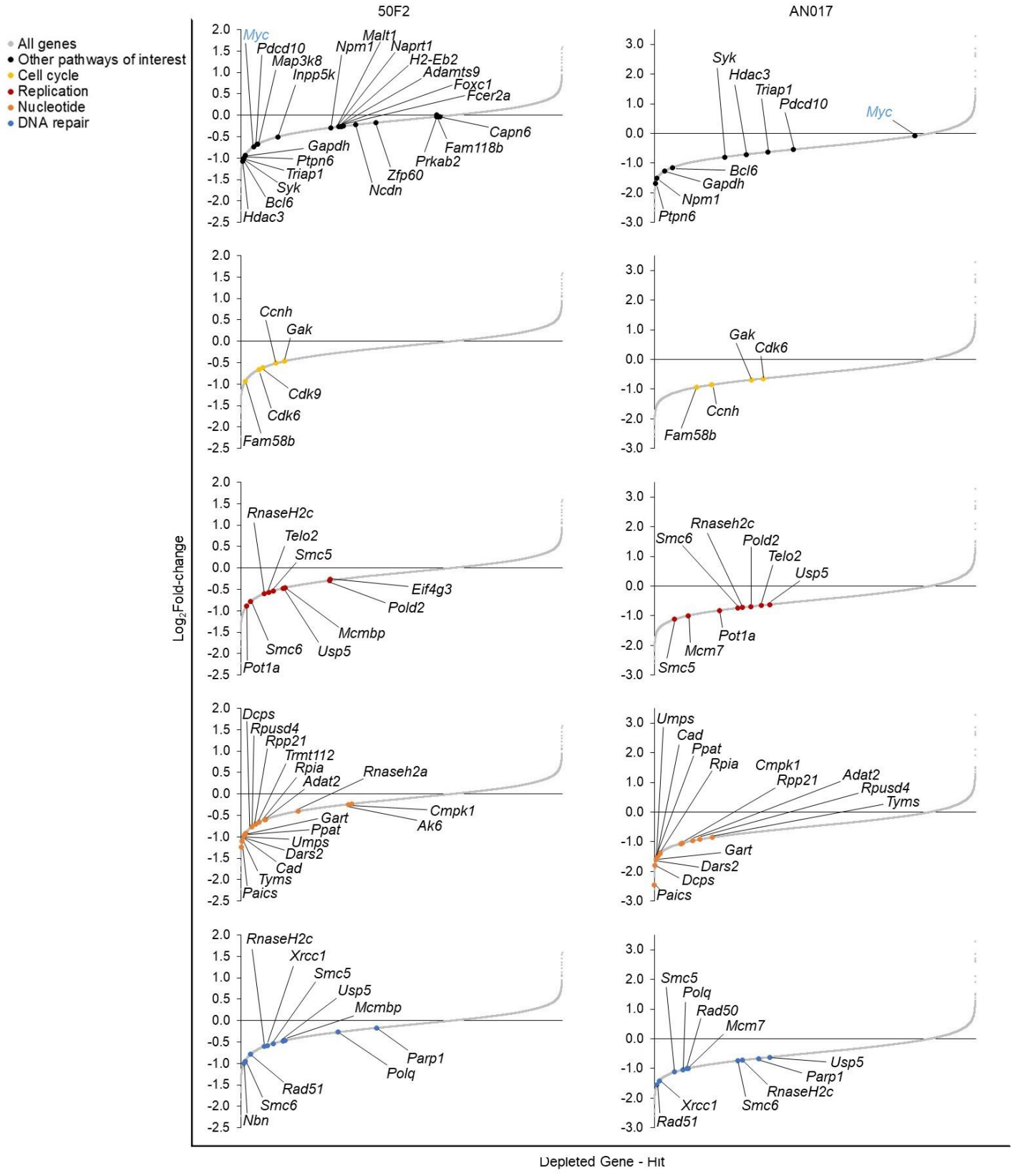

Identification of potential therapeutic targets for *Atm*$^{-/-}$*nu*$^{-/-}$ lymphomas by genome-scale CRISPR/Cas9-mediated loss-of-function screen of two cell lines established from *Atm*$^{-/-}$*nu*$^{-/-}$ lymphomas (50F2 and AN017) with an FDR <0.05. Constituent genes of each of the most significantly affected biological processes identified by RNA-seq, were depleted in both lymphoma cell lines and present potential therapeutic targets.

Figure S5. Nucleotide depletion induces cytotoxicity in *Eμ-Myc* lymphoma and replication stress in MYC-dependent *Atm*$^{-/-}$*nu*$^{-/-}$ lymphomas

A

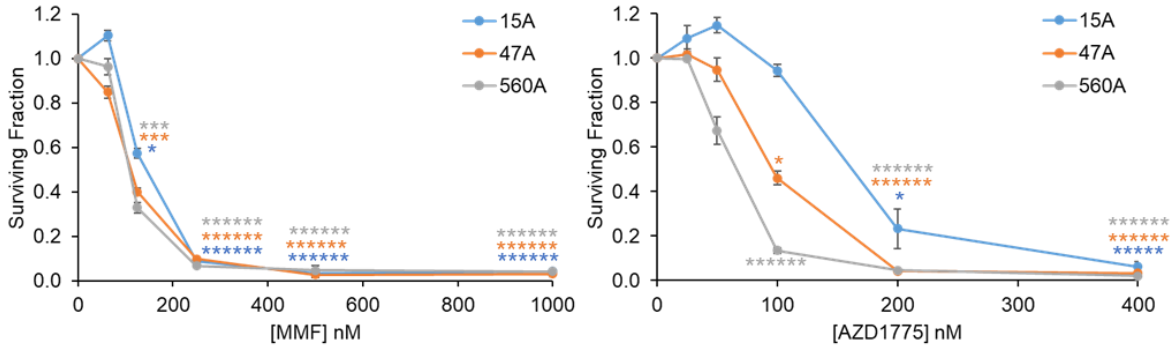

B

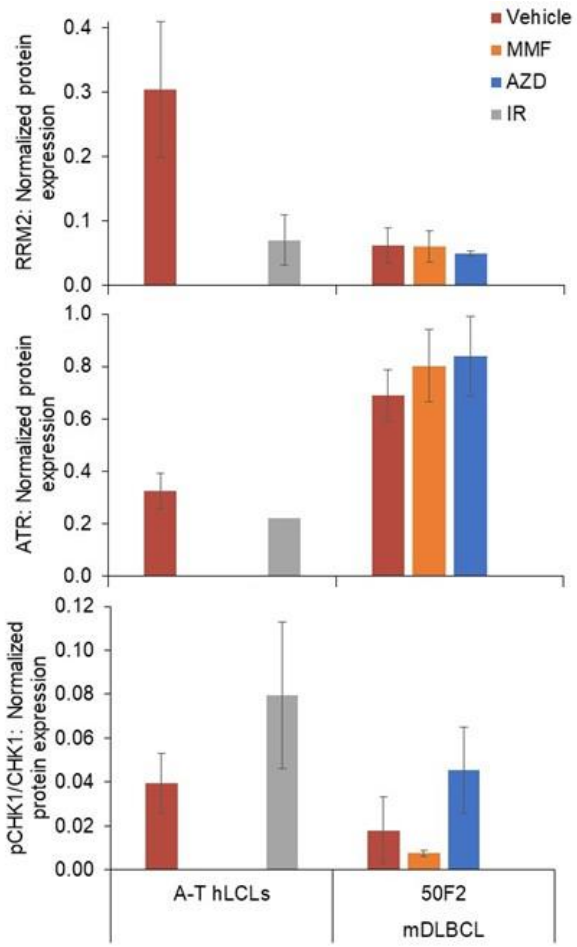

C

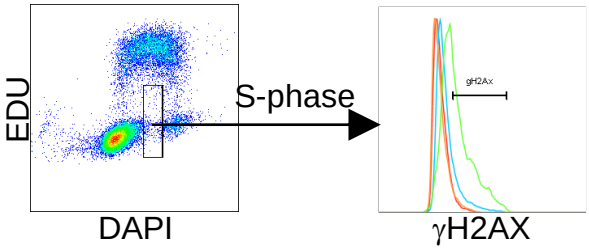

(A) Exposure (72h) of 3 *Atm* wild-type, *Eμ-Myc*-driven lymphoma cell lines to inhibitors of nucleotide synthesis (MMF or AZD1775; n=3) indicates sensitivity to both treatments as measured by Annexin V FACS analysis. Data presented as mean ± SEM. Statistical significance versus untreated controls (*), was ascertained by repeat-measures matched multi-comparison one-way ANOVA with Tukey post-hoc test and denoted by: *P≤0.05, **P≤0.01, ***P≤0.005, ****P≤0.001, *****P≤0.0005, ******P≤0.0005. (B) In comparison to human ATM-deficient non-tumor (three A-T patient-derived LCL) controls, basal RRM2 protein expression and a replicative stress indicator (phosphorylated CHK1 to total CHK1 protein ratio) are lower in a representative cell line established from an *Atm*$^{-/-}$*nu*$^{-/-}$ lymphoma (50F2) whilst ATR is elevated. IR-induced (6Gy, 30min) replication stress in the A-T patient-derived LCL resulted in reduced RRM2 expression and concurrent elevated CHK1 phosphorylation which was replicated upon AZD1775 (500nM) but not MMF (250nM) treatment (72h) of an *Atm*$^{-/-}$*nu*$^{-/-}$ lymphoma (50F2). Band intensities quantified using Image J were normalized to VINCULIN from ≥3 western blots and presented as mean ± SEM. (C) The proportion of γH2AX^{+} cells in non-replicating (inactive, quiescent) S-phase was determined by flow cytometry. Cell cycle stage was identified by DAPI staining and replicating cells by EDU. The dot plot illustrates the gating strategy employed to select non-replicating (EDU^{-}) cells residing in S-phase in a representative vehicle-treated sample. The γH2AX expression of EDU^{-} S-phase cells treated with vehicle (red), MMF (orange), AZD1775 (blue) or MMF + AZD1775 combined (green) cells on the right clearly demonstrates the accumulation of γH2AX in non-replicating S-phase cells (EDU^{-} γH2AX^{+}) following combination treatment.

Figure S6. Elevated MYC expression sensitizes human DLBCL cells to nucleotide depletion

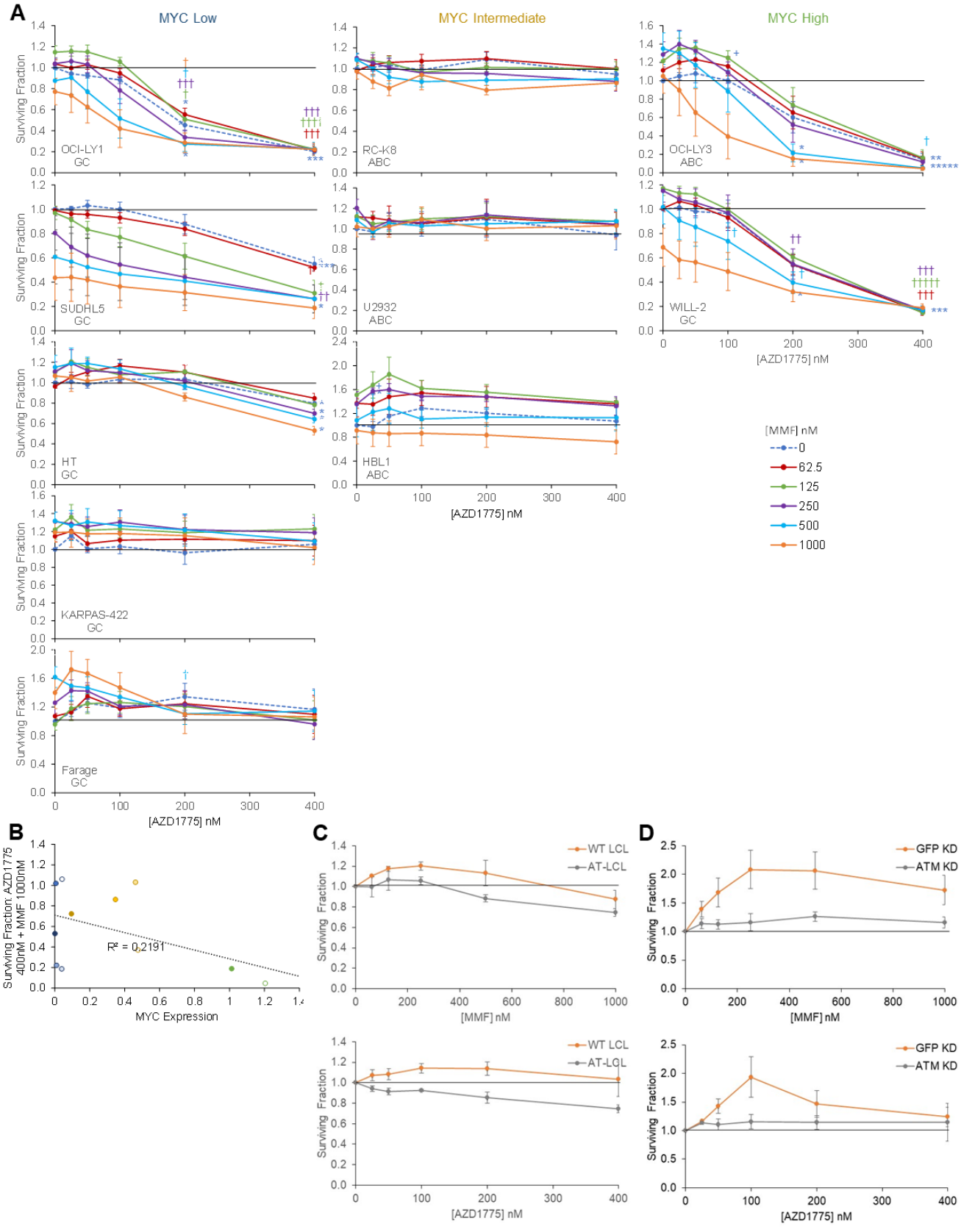

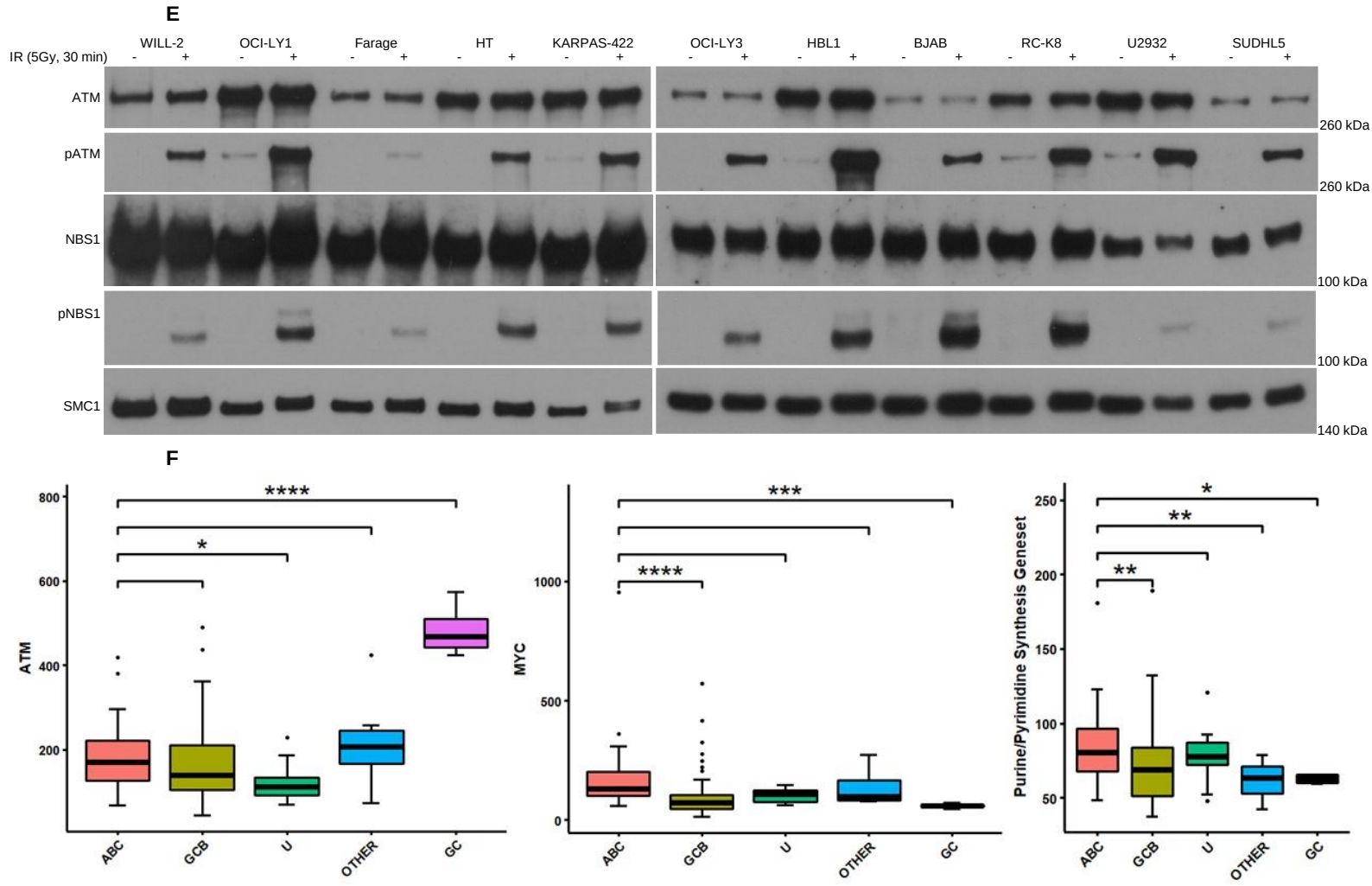

(A,B) Exposure (72h) of 11 human DLBCL cell lines with varying degrees of MYC expression to inhibitors of nucleotide synthesis (MMF or AZD1775; n=5) indicated a trend between MYC expression and increased cytotoxicity as measured by CellTitre-Glo for WEE1 inhibition (AZD1775). (C,D,E) Sensitivity to nucleotide synthesis inhibition is ATM-independent as evidenced by lack of differential sensitivity in (C) LCL cells derived from three healthy volunteers (WT LCL) versus three A-T patients (AT LCL) and (D) shRNA-ATM-KD CII cells (CLL tumor cell lines) and also (A,E) non-responsiveness of the sole cell line exhibiting loss of functional ATM (Farage); assessed by lack of multiple parameters of functional activity following irradiation (IR, 5 Gy, 30 min) of the cell lines. Samples were run on two separate gels. (F) Comparison of human DLBCL subsets and germinal centers by data-mining published human DLBCL RNA-seq datasets of human ABC DLBCL[7] (n=32), GCB DLBCL[7] (n=54), U DLBCL (n=10), Other DLBCL (n=8) and healthy control GC B-cells[8] (n=4). In comparison to GC B-cells, patient ABC DLBCL expresses significantly reduced *ATM* whilst expression of both *MYC* and a purine/pyrimidine biosynthesis gene-set is higher in ABC-DLBCL than GC B-cells and GCB DLBCL. ABC, activated B-cell-like; GCB, germinal center

B-cell-like; U, unknown; Other, other; GC, germinal center B-cells. Statistical significance versus (A) untreated controls (*), AZD1775 (+) or MMF (†) concentration as denoted by symbol color, (C,D) untreated controls (*) or WT or GFP KD (+) as denoted by color, was ascertained by repeat-measures matched multi-comparison two-way ANOVA with Tukey post-hoc test and denoted by: *$P \leq 0.05$, **$P \leq 0.01$, ***$P \leq 0.005$, ****$P \leq 0.001$, *****$P \leq 0.0005$.

Figure S7. Human Burkitt lymphoma cells exhibiting high MYC expression are sensitive to nucleotide depletion

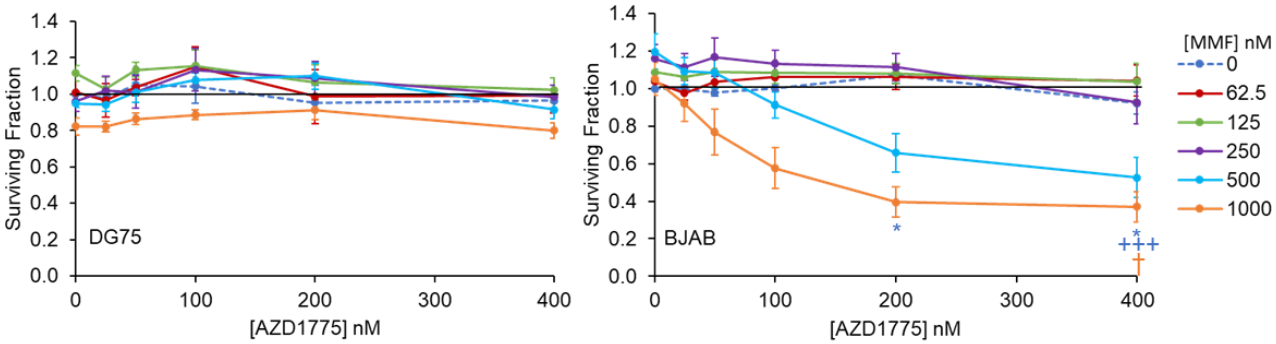

Exposure (72h) of human Burkitt lymphoma cell lines to inhibitors of nucleotide synthesis (MMF or AZD1775; n=5) indicates sensitivity to combined AZD/MMF treatment in BJAB (high MYC) but not DG75 (low MYC) (Figure S6E).[19] Statistical significance versus untreated controls (*), AZD1775 (+) or MMF (†) concentration as denoted by symbol color, was ascertained by repeat-measures matched multi-comparison two-way ANOVA with Tukey post-hoc test and denoted by: *P≤0.05, **P≤0.01, ***P≤0.005, ****P≤0.001, *****P≤0.0005.

References

1. Liao MJ, Yin C, Barlow C, Wynshaw-Boris A, van Dyke T. Atm is dispensable for p53 apoptosis and tumor suppression triggered by cell cycle dysfunction. Mol Cell Biol. 1999;19(4):3095-3102.

2. Weston VJ, Oldreive CE, Skowronska A, et al. The PARP inhibitor olaparib induces significant killing of ATM-deficient lymphoid tumor cells in vitro and in vivo. Blood. 2010;116(22):4578-4587.

3. Adams JM, Harris AW, Pinkert CA, et al. The c-myc oncogene driven by immunoglobulin enhancers induces lymphoid malignancy in transgenic mice. Nature. 1985;318(6046):533-538.

4. Stankovic T, Stewart GS, Fegan C, et al. Ataxia telangiectasia mutated-deficient B-cell chronic lymphocytic leukemia occurs in pregerminal center cells and results in defective damage response and unrepaired chromosome damage. Blood. 2002;99(1):300-309.

5. Young LA, O'Connor LO, de Renty C, et al. Differential Activity of ATR and WEE1 Inhibitors in a Highly Sensitive Subpopulation of DLBCL Linked to Replication Stress. Cancer Res. 2019;79(14):3762-3775.

6. Oldreive CE, Skowronska A, Davies NJ, et al. T-cell number and subtype influence the disease course of primary chronic lymphocytic leukaemia xenografts in alymphoid mice. Dis Model Mech. 2015;8(11):1401-1412.

7. Morin RD, Johnson NA, Severson TM, et al. Somatic mutations altering EZH2 (Tyr641) in follicular and diffuse large B-cell lymphomas of germinal-center origin. Nat Genet. 2010;42(2):181-185.

8. Beguelin W, Popovic R, Teater M, et al. EZH2 is required for germinal center formation and somatic EZH2 mutations promote lymphoid transformation. Cancer Cell. 2013;23(5):677-692.

9. Liao Y, Smyth GK, Shi W. The Subread aligner: fast, accurate and scalable read mapping by seed-and-vote. Nucleic Acids Res. 2013;41(10):e108.

10. Robinson MD, McCarthy DJ, Smyth GK. edgeR: a Bioconductor package for differential expression analysis of digital gene expression data. Bioinformatics. 2010;26(1):139-140.

11. Subramanian A, Tamayo P, Mootha VK, et al. Gene set enrichment analysis: a knowledge-based approach for interpreting genome-wide expression profiles. Proc Natl Acad Sci U S A. 2005;102(43):15545-15550.

12. Mootha VK, Lindgren CM, Eriksson KF, et al. PGC-1alpha-responsive genes involved in oxidative phosphorylation are coordinately downregulated in human diabetes. Nat Genet. 2003;34(3):267-273.

13. Davies NJ, Kwok M, Gould C, et al. Dynamic changes in clonal cytogenetic architecture during progression of chronic lymphocytic leukemia in patients and patient-derived murine xenografts. Oncotarget. 2017;8(27):44749-44760.

14. Jacobsson B, Bernell P, Arvidsson I, Hast R. Classical morphology, esterase cytochemistry, and interphase cytogenetics of peripheral blood and bone marrow smears. J Histochem Cytochem. 1996;44(11):1303-1309.

15. Zhang H, Meltzer P, Davis S. RCircos: an R package for Circos 2D track plots. BMC Bioinformatics. 2013;14:244.

16. Da Costa D, Agathanggelou A, Perry T, et al. BET inhibition as a single or combined therapeutic approach in primary paediatric B-precursor acute lymphoblastic leukaemia. Blood Cancer J. 2013;3:e126.

17. Wright G, Tan B, Rosenwald A, Hurt EH, Wiestner A, Staudt LM. A gene expression-based method to diagnose clinically distinct subgroups of diffuse large B cell lymphoma. Proc Natl Acad Sci U S A. 2003;100(17):9991-9996.

18. Liberzon A, Birger C, Thorvaldsdottir H, Ghandi M, Mesirov JP, Tamayo P. The Molecular Signatures Database (MSigDB) hallmark gene set collection. Cell Syst. 2015;1(6):417-425.

19. Barnouin K, Fredersdorf S, Eddaoudi A, et al. Antiproliferative function of p27kip1 is frequently inhibited in highly malignant Burkitt's lymphoma cells. Oncogene. 1999;18(46):6388-6397.

Supplementary Tables provided as Excel files except Table 2.

Table S1. Classification features of *Atm*$^{-/-}$*nu*$^{-/-}$ tumors

Microsoft Excel Table S1

Note: DLBCL, NOS, diffuse large B-cell lymphoma, not otherwise specified; +, present; ND, not done; -, not present; NA, not amplified; ~, undetermined; M, mutated; UM, unmutated.

Table S2. Cytogenetic profiles of $Atm^{-/-}nu^{-/-}$ diffuse large B-cell lymphoma, not otherwise specified (DLBCL, NOS) tumors

Tumor code	M-FISH Cytogenetic aberrations	Number of analysed cells	Targeted FISH *Myc* copy number	*IgH* translocation	*IgH* loss
703	36~41, XX, der(X)t(X;13)[11], der(13)t(13;18)[9], der(18)t(18;X)[8], +6[4], -X[8], -4[4], -3[3], -5[5], -13[3], -15[3], -16[4], -17[4], -18[4], -19[3], add(6)[4], der(X)t(X;6)[3]	36	2	No	No
5F3	39~40, XX, der(17)t(11;17)[19], -11[17], -16[15], add(6)[15], dup(14)[5], der(18)t(15;12;18)*[8], der(18)t(15;18)*[8], der(6)t(1;6), der(1)t(1;16)[3]	20	3	No	Monoallelic *IgH V1*
593	39~40, XY, der(17)t(15;17)[19], -Y[6], -11[3], dup(4)[6], add(4)[6], der(13)t(3;13)[7], der(5)t(5;4)[4]	20	2	No	*IgH*
37M3	30~40, XY, der(18)t(12;18)[6], der(18)t(8;18)[4], der(18)t(5;18)[3], der(18)t(7;18)[3], -12[5], dup(18)[4], add(1)[3], add(3)[3], add(5)[3], add(11)[3], t(1;2)[5]	40	2	No	No
50F2	30~41, XX, dup(18)der(18)t(7;18)[12], -19[5], -5[4], -7[4], -8[4], -9[4], -2[3], -12[3], -16[3]	20	2	No	No
68F2	40, XX (Normal)[4]/40~41, XX, der(12)t(12;15)[8], -19[5], +3[5], +12[5], der(19)t(12;19)[3]	12	3	Yes	No

Note: FISH, fluorescence in-situ hybridization; M-FISH, multicolor-FISH; [#], denotes the number of cells in which the abnormality was detected;

*, Due to technical limitations of M-FISH analysis these aberrations have been denoted separately but could potentially be the same.

Table S3. RNA-seq: Significantly differentially expressed genes

Microsoft Excel Table S3

Note: baseMean, mean of normalized counts of all samples; log2FoldChange, effect size estimate of the expression change between comparison and control groups; lfcSE, standard error of the log2FoldChange; stat, Wald-log test statistic; pvalue, raw p-value; padj, false discovery rate p-value; 1-593.bam; *Atm*$^{-/-}$*nu*$^{-/-}$ lymphoma sample (593 replicate 1) bam files; plus.minus.bam, control *Atm*$^{+/-}$*nu*$^{-/-}$ splenic B-cell bam file; plus.plus.bam, control *Atm*$^{+/+}$*nu*$^{-/-}$ splenic B-cell bam file.

Table S4. RNA-seq Kyoto Encyclopaedia of Genes and Genomes (KEGG) pathway analysis: Upregulated gene expression pathways

Microsoft Excel Table S4

Note: ID, unique identifier for each KEGG object; GeneRatio, fraction of differentially expressed genes found in the gene set; BgRatio, fraction of differentially expressed genes annotated to a pathway; p.adjust, corrected p-value using false discovery rate methods; qvalue, p-value using multiple hypothesis test correction indicates the probability that a reaction module was identified by chance; geneID, EntrezGene ID; Count, number of genes enriched in a KEGG pathway; Log_pvalue, $\log_{10}$ of the p-value; Log_qvalue, $\log_{10}$ of the q-value; Log_padjust, $\log_{10}$ of the p.adjust-value.

Table S5. RNA-seq Kyoto Encyclopaedia of Genes and Genomes (KEGG) pathway analysis: Downregulated gene expression pathways

Microsoft Excel Table S5

Note: ID, unique identifier for each KEGG object; GeneRatio, fraction of differentially expressed genes found in the gene set; BgRatio, fraction of differentially expressed genes

annotated to a pathway; p.adjust, corrected p-value using false discovery rate methods; qvalue, p-value using multiple hypothesis test correction indicates the probability that a reaction module was identified by chance; geneID, EntrezGene ID; Count, number of genes enriched in a KEGG pathway; Log_pvalue, $\log_{10}$ of the p-value; Log_qvalue, $\log_{10}$ of the q-value; Log_padjust, $\log_{10}$ of the p.adjust-value.

Table S6. RNA-seq Gene Set Enrichment Analysis (GSEA): Upregulated hallmarks

Microsoft Excel Table S6

Note: pval, nominal p value, the statistical significance of the enrichment score that is of limited use in comparing gene sets; padj, false discovery rate p-value; ES, enrichment score for the gene set, the degree to which this gene set is overrepresented at the top or bottom of the ranked list of genes in the expression dataset; NES, normalized enrichment score for the gene set; nMoreExtreme, number of times a control gene set had a more extreme enrichment score value, used to calculate nominal p-value; Size, number of genes present in the expression dataset; leadingEdge, subset of genes that contribute most to the ES.

Table S7. Clustered regularly interspaced short palindromic repeats (CRISPR): Comparison of sgRNA target gene expression at Day 18 vs Day 0 in two A-T DLBCL derived cell-lines

Microsoft Excel Table S7

Note: Score, MAGeCK Robust Rank Aggregation (RRA) enrichment score indicates the essentiality of a gene to identify ‘hits’; FDR, false discovery rate.

Table S8. Clustered regularly interspaced short palindromic repeats (CRISPR) KEGG pathway analysis: Depleted gene (Hit) expression pathways

Microsoft Excel Table S8

ID, unique identifier for each Kyoto Encyclopaedia of Genes and Genomes (KEGG) object; Observed gene Count, number of identified depleted genes in the KEGG pathway; Background gene Count, number of total genes in the KEGG pathway; FDR, false discovery rate; geneID, EntrezGene ID.